Hydrogen evolution on non-metal oxide catalysts

JPhys Energy

TOPICAL REVIEW • OPEN ACCESS

Hydrogen evolution on non-metal oxide catalysts

IOP Publishing J. Phys. Energy 2 (2020) 042002 https://doi.org/10.1088/2515-7655/aba3bc

Journal of Physics: Energy

OPEN ACCESS

RECEIVED
13 March 2020

REVISED
19 May 2020

ACCEPTED FOR PUBLICATION
7 July 2020

PUBLISHED
12 August 2020

TOPICAL REVIEW

Hydrogen evolution on non-metal oxide catalysts

Stephen Rhatigan[1], **Marie-Clara Michel**[1,2] **and Michael Nolan**[1,3]

[1] Tyndall National Institute, UCC, Lee Maltings, Dyke Parade, Cork T12 R5CP, Ireland
[2] School of Chemistry, University College Cork, Cork, Ireland
[3] Author to whom any correspondence should be addressed.

E-mail: Michael.nolan@tyndall.ie

Keywords: hydrogen, phosphides, chalcogenides, water splitting

Abstract

Water splitting to produce hydrogen gas, using renewably produced electricity (electrocatalysis) or by direct conversion of solar energy (photocatalysis), is a strategy that addresses key environmental and energy challenges. The overall water splitting reaction proceeds as two half reactions, namely the oxygen evolution reaction (OER) and hydrogen evolution reaction (HER), each of which require catalysts specifically tailored to maximize efficiency. The benchmark catalysts for the HER are noble metals. However, their expense and rarity makes them economically unfeasible for large-scale H_2 production from water. Consequently, there are considerable efforts to find cheap, abundant materials that can efficiently catalyze the HER. Over the last decade, metal chalcogenides and phosphides have emerged as promising candidates for HER. In this review article, we discuss a selection of the multitude of studies and materials in these two classes of catalyst to give a flavor of the relevant developments and properties of these materials. In addition to the selection of catalyst materials, preparation and structuring are playing a strong role in enhancing HER and overcoming fundamental challenges. The role of modeling in the performance of HER catalysts is also discussed and we end with a short perspective on the key attributes of a good HER catalyst.

1. Introduction

The development of clean, renewable energy systems is of the utmost importance to address the issues of climate change and rising global energy demands. With a rapidly rising world population, the global primary energy-consumption rate is expected to increase from 17 TW in 2010 to 27 TW by 2040 [1]. Renewable energy sources, such as solar, wind, and wave energy, are intermittent and often location specific. These constraints necessitate an efficient means for storage and transport of excess energy produced at peak times for reintroduction to the grid where and as required. This excess energy is best stored in a form that is transportable and is itself clean.

Water splitting, to produce hydrogen gas (H_2), is an attractive prospect for a variety of reasons. H_2, produced from water using renewably produced electricity, via electrocatalysis, or by direct conversion of solar energy, via photocatalysis or photoelectrochemistry, offers a zero emissions fuel. H_2 has a lower heating value (120 MJ kg^{-1}) almost three times that of gasoline (44 MJ kg^{-1}) [2] and the only by-product of its combustion or recombination with oxygen in a fuel cell is water.

To make H_2 fuel competitive, it must be produced at a cost of less than \$4 kg^{-1} of H_2 [3, 4]. If we consider using solar to produce hydrogen, the US Department of Energy reported that their solar to hydrogen (STH) efficiency target for realistic application of hydrogen production from photocatalytic water splitting is 5%, which would allow a cost of \$4.6 kg^{-1} for hydrogen generation, which is very close to the \$4 kg^{-1} target. Improvements in the efficiency of the hydrogen evolution reaction (HER) will substantially drive down the cost. In addition, the European Strategic Energy Technologies Roadmap points out that new and enhanced catalysts are required [5].

The water splitting reaction, whether electro- or photocatalytically driven, proceeds as two half reactions; the oxygen evolution reaction (OER) and the HER are oxidation and reduction reactions, respectively. The HER proceeds at the (photo)cathode, for which the most efficient materials are platinum-group metals,

PGMs. PGMs are critical materials with low abundance on earth, suffering from geopolitical issues around sourcing and are therefore extremely expensive. These issues limit the large-scale implementation and economic viability of water splitting technologies. This context has spurred significant scientific efforts toward the development of cheap, earth-abundant materials that can efficiently catalyse the HER. The last 15 years has seen a surge of interest in metal chalcogenides (sulfide, selenides, and tellurides) and phosphides as catalysts for HER, showing high activity and good stability in acidic media and over multiple cycles. An account of recent progress in this endeavor, to give the interested reader a perspective on the properties and HER activity of these non-metal oxide materials, is the subject of the present review.

2. Fundamentals of hydrogen production from water splitting

The overall water splitting reaction may be expressed as follows [6]:

$$2H_2O \rightarrow 2H_2 + O_2$$

The expressions which describe the two half reactions, OER and HER, depend on the conditions under which the reaction takes place. In neutral or alkaline conditions, the half reactions are [6, 7]:

$$\text{OER, anode}: \quad 2OH^- \rightarrow \frac{1}{2}O_2 + H_2O + 2e^-$$

$$\text{HER, cathode}: 2H_2O + 2e^- \rightarrow H_2 + 2OH^-$$

While in acidic conditions, the oxidation and reduction reactions may be expressed as [6, 7]:

$$\text{OER, anode}: \quad 2H_2O \rightarrow O_2 + 4H^+ + 4e^-$$

$$\text{HER, cathode}: \quad 4H^+ + 4e^- \rightarrow 2H_2$$

Water splitting can be achieved electrochemically, where the impetus for the reaction is provided by the potential bias between the electrodes. The ideal thermodynamic voltage required to drive water splitting is 1.23 V at 298 K and 1 atm [6]. However, in practice, due to losses, kinetic barriers and non-idealities in the catalysts, larger voltages are required. The difference between the thermodynamic and the applied potential is known as the overpotential and it has contributions arising from activation barriers at the anode and cathode surfaces, among other considerations. This renders the HER and, particularly, the OER sluggish and necessitates catalysts to reduce the anodic and cathodic activation barriers and increase reaction rates. For the remainder of this review, we restrict our focus to the HER, and for the most part, in acidic conditions as this enhances the HER activity [8, 9]; the reverse is true for OER [10]. Moreover, the mechanism for HER in alkaline media is not as well understood [7]. However, progress in the development of HER catalysts that operate in alkaline media has been the subject of a number of recent reviews [11, 12].

The HER proceeds at the cathode in a two-step process and there are two possible pathways: the Volmer–Tafel reaction and the Volmer–Heyrovsky reaction [13]. The Volmer step is common to both pathways and may be described as:

$$\text{Volmer}: \quad H^+ + e^- \rightarrow H_{ads}$$

This is called the 'discharge step' as an electron is transferred to a proton at the cathode surface, resulting in a surface bound H species, i.e. H_{ads}. The second step involves desorption, and is described by the Tafel or Heyrovsky reactions:

$$\text{Tafel}: \quad H_{ads} + H_{ads} \rightarrow H_2$$

$$\text{Heyrovsky}: \quad H_{ads} + H^+ + e^- \rightarrow H_2$$

The adsorption (discharge) step competes with the desorption steps and the optimal catalyst will strike a balance between these processes. This balance may be characterized by the Gibbs free energy of adsorption of a H atom (ΔG_H) at the catalyst surface [14]. This quantity is widely accepted as a descriptor for the HER activity of a catalyst and may be computed from first principles via density functional theory (DFT) using:

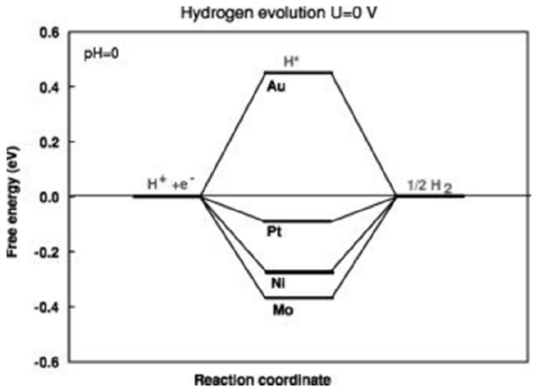

Figure 1. Free energy diagram for hydrogen evolution at various metal surfaces, with no applied potential, (U = 0). The modeled conditions correspond to standard temperature and pressure (STP: 300 K, 1 bar) and pH = 0. By definition, the free energy of $H^+ + e^-$ is the same as that of $^1/_2$ H_2 at standard conditions. The free energies of adsorption are computed with DFT and corrected for entropy and zero point energies. Coverages of 1/4 are used. Reproduced with permission from [15], © 2005 ECS.

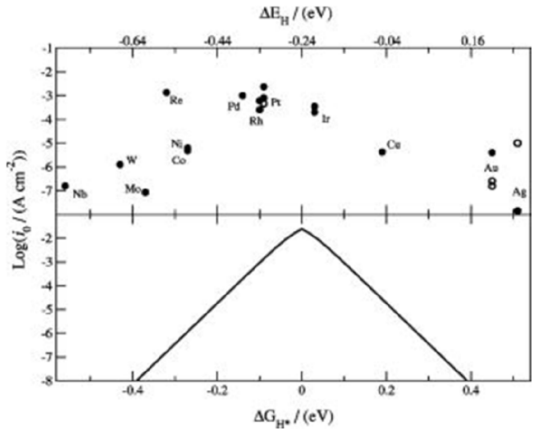

Figure 2. The top panel shows experimentally measured exchange current, $\log(i_0)$, for HER at metal surfaces plotted against the DFT calculated hydrogen chemisorption energy per atom, ΔE_H (top axis). The bottom panel shows a volcano plot which arises from a simple kinetic model of the exchange current plotted against the free energy for hydrogen adsorption, $\Delta G_H = \Delta E_H + 0.24$. Reproduced with permission from [15], © 2005 ECS.

$$\Delta G_H = \Delta E_{DFT} + \Delta ZPE - T\Delta S$$

where ΔE_{DFT}, is the thermodynamic energy difference between the initial and final (H_{ads}) state, computed with DFT; ΔZPE accounts for zero-point energy corrections; and the $T\Delta S$ term contains entropic contributions. Large, positive ΔG_H implies that adsorption is the difficult step whereas large, negative values of ΔG_H indicate strong adsorption of hydrogen and therefore render the desorption step difficult. Thus, consistent with the Sabatier principle, the optimal value for ΔG_H is close to 0 eV, and indeed, this is the case for the benchmark catalyst, Pt, as shown in figure 1 and compared to other metals.

There are measured quantities that can quantify the intrinsic HER activity of a material. One such parameter is the turnover frequency (TOF) of an active site, which, as the name suggests, is the number of reactions per unit time. The surface of a given catalyst material will present sites of different types, with variations that depend on factors including ion species, coordination, edge sites, and defects. In principle, each site will have an intrinsic activity or TOF, but this is not measurable by experimental means. Instead, practical approaches estimate the average per site TOF, based on measurements of total electrode activity and the number of active sites, or site density, SD [16, 17]. Thus, the challenge in evaluating and comparing the intrinsic activities of materials for HER depends on reliable, standardized measurements of the SD.

Strategies for determining the number of catalytic sites include measurements of the specific catalyst surface area *via* electrochemical techniques, such as capacitance measurements, or gaseous adsorption methods, such as BET, among others [18]. These approaches are based on the reasonable assumption that the number of active sites will scale with the surface area. However, they are not applicable to all materials and their accuracy can be hindered by differences in the availability and accessibility of active sites between

measurement and HER conditions. This, in turn, makes TOF a challenging parameter to evaluate conclusively, in a way that admits comparison between materials.

Thus, many researchers omit intrinsic activity measurements and opt instead for total electrode activities as the metric to assess the catalyst performance. The quantities used for the measurement of total electrode activity, described below, depend on multiple factors, including intrinsic activity, specific surface area, catalyst loading, substrate, and other effects [16]. This means that, for a given material, they can be optimized through electrode preparation and design. Hence, a material with high intrinsic activity may not perform as well as an intrinsically less active material when using total electrode metrics, due to sub-optimal electrode design.

Two quantities commonly used when comparing the total electrode activity of HER catalysts are the Tafel slope and the overpotential [7, 9]. A Tafel plot relates the overpotential (η) to $\log_{10}$ of the measured current density (j), via:

$$\eta = m\log_{10} j + c$$

The rate-limiting step of the HER is elucidated from the slope of the Tafel plot, represented by m in the above formula. Typically, values for the Tafel slope of 120, 30, and 40 mV dec^{-1} indicate that the Volmer, Tafel, and Heyrovsky steps, respectively, determine the rate of reaction [19]. A small Tafel slope is a desirable quality in a catalyst because this indicates a large change in the current density, in response to small increments in the overpotential.

Another important quantity which emerges from the Tafel plot is the exchange current density, j_0, which is the current density at equilibrium conditions ($\eta \to 0$). This quantifies the ability of a material to catalyze the HER and the best catalysts will exhibit high j_0.

The overpotential, denoted η_j, and measured relative to the standard/reversible/normal hydrogen electrode (SHE/RHE/NHE), is that potential required to produce a current density, j [16]. This value for the current density corresponds to the current per unit area of the electrode and is typically chosen as 10 mA cm^{-2}, by convention. This convention is used because this current density in a PEC cell corresponds to an STH efficiency of approximately 10% [9, 20]. To avoid the complications of sign, only the magnitudes of η_j will be quoted in this review. The area is simply the geometric area of the electrode and neglects intricacies of the electrode surface. Consequently, considerations such as surface nanostructuring and catalyst loadings are not taken into account.

For comparison purposes, we will refer to the Tafel slope, the overpotential, η_j, and in some cases the exchange current density, j_0, should these values be provided in the cited study. A detailed account of these quantities can be found in a review by Anantharaj and colleagues [21].

For stability tests, some common approaches are to compare the performance of the catalyst after ~1000–20 000 voltammetry (CV) cycles or to measure variations in the overpotential (current density) required to maintain continuous performance at a fixed current density (overpotential) for N hours [22]. Measurements are referred to as potentiostatic/galvanostatic where the overpotential/current density are maintained constant. Details of these tests will also be included.

The quantities ΔG_H and j_0 establish a crucial link between computational and experimental results, which can be illustrated using a 'volcano plot' [15]. The volcano plot in figure 2 shows experimentally measured j_0 for a variety of metals plotted against their computed values for ΔG_H. The Pt-group metals are clustered at the top of the volcano, exhibiting high values for j_0, and computed ΔG_H close to 0 eV. Reactive metals, at which H adsorbs too strongly, appear on the left of the volcano, while the unreactive metals appear on the right hand side.

Equipped with these descriptors, we have criteria against which we can assess the candidacy of a material to catalyse the HER. In particular, computational methods allow for high throughput screening of HER catalysts. However, while ΔG_H is a useful yardstick, other details of the HER should not be neglected. Such details include the catalyst surface area, availability of active sites, coverage effects and the nature of the real catalyst surface. For instance, H coverage can have a strong impact on the computed ΔG_H and must be accounted for when performing simulations of potential HER catalysts [23, 24]. As an example of the latter consideration, computing ΔG_H for a pristine metal surface loses relevance should that surface form an oxide layer under operating conditions.

Indeed, the issue of aligning computational models of catalyst surfaces with the physical systems, as they present under operating conditions, is profound. One consideration is the impact of the solvent, and computational approaches to describing the catalyst-electrolyte interface will be discussed in section 6 of this review. Moreover, the nature of the catalyst surface is dependent on its environment [25, 26] and *ex situ* characterization can fall short in the description of crucial surface features which emerge during operation.

For example, an x-ray absorption fine structure spectroscopic study of a PtO/TiO_2 catalyst during water splitting revealed differences in the catalyst structure between the *ex situ* and operating conditions [27].

Having identified PtO as the active site, the authors reported an increased Pt–O bond length, from 2.07 to 2.13 Å, and a decrease in the coordination number, from 4 to 2.5, for the catalyst *in operando*, relative to the catalyst *ex situ*, both before and after use.

The changes induced during operation can be significant, leading to the assertion from some authors that the term 'pre-catalyst' is more appropriate when referring to the *ex situ* materials [28, 29]. Despite this, it is often assumed that catalysts are stable under HER operating conditions and that *in situ* and *operando* analysis is more pertinent under harsh OER conditions [26]. While this assumption can be true, it should of course be the subject of rigorous testing. Deng and co-workers used *operando* Raman spectroscopy to confirm the consensus that S atoms are the active sites in the HER catalysis at amorphous MoS_x [30]. In addition, spatially resolved, *operando* measurements performed with scanning electrochemical cell microscopy (SECCM) indicate increased HER activity at edge sites of MoS_2 [31–33].

Zhang *et al* used post-catalysis analysis of Co_2P and reported that the composition of the electrode surface was largely unchanged in acidic conditions but degraded to hydroxides in alkaline conditions [34]. However, *in situ* x-ray absorption spectroscopy (XAS) measurements suggest that metallic cobalt is the active component for HER [35]. Starting from amorphous metallic Co nanoparticles in pH 7 potassium phosphate solution, the authors found that the metal/phosphate ratio varied with changes in the cathodic potential. Saadi *et al* used *operando* spectroscopic techniques to show that the active component in HER at CoP films in acidic conditions consisted of an amorphous material with Co in a near-zerovalent state and P in a reduced state [36]. Moreover, the authors reported considerable differences in the composition of the catalyst between *ex situ* and *operando* characterization.

Zhu *et al* used a combination of *operando* measurements, such as *in situ* XAS, Raman spectroscopy, and liquid-phase transmission electron microscopy to elucidate the nature of active sites of P-doped $CoSe_2$ in alkaline media under HER conditions [28]. The authors found that P-substitution facilitated the formation of defects, which exposed active, metallic Co sites for the HER.

Besides determining the true nature of the catalyst, *operando* measurements can be used to gain greater insight into the reaction pathway. Wang *et al* used *operando* nuclear magnetic resonance spectroscopy to elucidate the mechanism for the HER at anatase TiO_2 decorated with Pd nanoparticles [37]. Their study, which was supported by DFT calculations, yielded a detailed description of the key proton transfer steps involved in the HER, using methanol as a sacrificial hole scavenger.

In situ and *operando* spectroscopies continue to gain considerable traction in the study of catalysis and developments in this area have been the subject of recent reviews [25, 26]. These considerations should serve to embolden rather than dishearten. As the tools at our disposal increase the breadth of our understanding, so too will they inform refined computational models and fabrication methods for the rational design of new photocatalyst materials.

In this review, we describe non-oxide catalysts that show significant promise in the search for cheap, abundant, and efficient alternatives to noble metals for the HER. This is not an exhaustive review of all materials, but instead we focus on a selection of key catalyst materials and results that best highlight advances in this field, particularly from the perspective of how composition and structure can be used to promote the HER. We also include some results from DFT and machine learning that have been employed in deepening the understanding of HER materials.

As part of this discussion, we note that while metal oxides are perhaps the most widely studied class of materials for photocatalytic applications, e.g. TiO_2 or Fe_2O_3, they are unsuitable as HER catalysts as hydrogen binds too strongly to oxygen sites in the surface, thereby forming an unreactive hydroxyl layer. These catalysts, therefore, need a co-catalyst, such as Pt, or a sacrificial agent to consume electrons. Thus, the focus for HER is on non-noble transition metals and their compounds with elements from groups 13–16 of the periodic table. In this regard, we pay particular attention to the chalcogenides (S, Se, and Te) and phosphides, which have recently emerged as interesting candidates for HER catalysts.

3. Hydrogen evolution reactions on metal chalcogenides

Metal chalcogenides, particularly layered transition metal dichalcogenides (TMDs) containing sulfur or selenium, have generated great interest for their catalytic activity toward HER. As they are useful for hydrodesulfurization (HDS) chemistry [38, 39], they are also of great interest for HER given that the key reaction steps are similar between both chemistries. Perhaps the most widely studied of these materials is MoS_2. While bulk MoS_2 [7, 40] and the basal planes [41] were found to be inactive, other studies have examined the catalytic performance of MoS_2 supported on substrates [42, 43]. MoS_2 dispersed at an NiS_x surface promoted HER and inhibited degradation of the catalyst; the MoS_2 pigmented catalysts operated with overpotentials 50–100 mV below that recorded for bare NiS_x [42]. MoS_2 supported on silica also exhibited good hydrogen evolution properties [43]. Drawing inspiration from these studies and noting

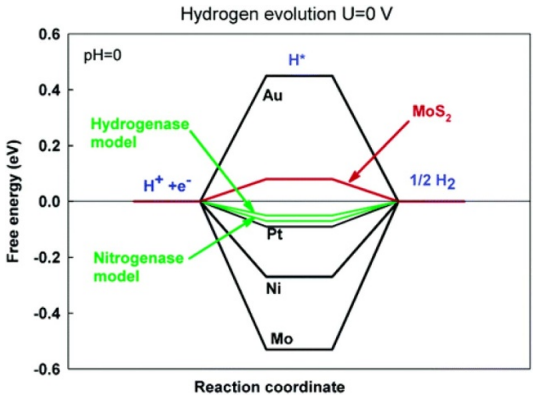

Figure 3. Computed free energy for HER at STP and a potential of U = 0 vs. SHE, with pH = 0. The result for MoS_2 is the free energy required to increase the hydrogen coverage from 25% to 50%. Reproduced with permission from [44], © 2005 American Chemical Society.

Table 1. Selected data taken from [46] and [47]. For details of the precise surfaces and H coverage, the reader should consult the original papers.

Ref	Material	Site	ΔG_H (eV)
[46]	MoS_2	Mo-edge	0.08
		S-edge	0.18
	Co-Mo-S	S-edge	0.10
	WS_2	W-edge	0.22
		S-edge	0.22
	Co-W-S	S-edge	0.07
[47]	MoS_2	Mo-edge	0.06
		S-edge	−0.45
	WS_2	W-edge	−0.04
		S-edge	−0.06
	MoSe2	Mo-edge	−0.04
		Se-edge	−0.05
	WSe2	W-edge	0.17
		Se-edge	−0.05

similarities with the active site of nitrogenase, an enzyme which efficiently catalyzes the HER, Heinemann and colleagues presented a now widely cited computational investigation of MoS_2 as a HER catalyst [44]. This paper can be considered as the beginning of the high level of activity in discovering sulfides for the HER. The authors identified low-coordinated S-sites of the MoS_2 edge as active sites with ΔG_H comparable to that computed for Pt, as shown in figure 3.

WS_2 has the same layered structure as MoS_2, and has also been studied for its hydrogen evolution properties and corrosion resistance [45]. Silica-supported WS_2 was shown to be an active and stable catalyst for HER; 0.2 mg of the WS_2/SiO_2 catalyst yielded in excess of 0.2 ml h^{-1}, with a small drop in performance after 2 h [45]. Conversely, the Pt/SiO_2 catalyst produced 0.1 ml in the first hour, but only 0.04 ml in the second hour. A combined experimental and computational study of MoS_2 and WS_2 nanoparticles found WS_2 to be almost as active as MoS_2 [46]. Tafel slopes of 120 mV dec^{-1} and 135 mV dec^{-1} were recorded for MoS_2 and WS_2 catalysts, respectively. The authors also reported promotion of HER after incorporation of Co into the S-edges of both materials. The Tafel slope decreased to 101 mV dec^{-1} and 132 mV dec^{-1} for Co-promoted MoS_2 and WS_2. The computational results of this paper are summarized in table 1.

A subsequent study of MoS_2 and WS_2 by the same group adopted a more thorough approach and examined the effects of S- and H-coverage [47]. Consequently, the computational results for ΔG_H were revised and these results are also presented in table 1. The authors found that H binding was too strong at the S-edge of MoS_2, even at the highest possible coverage. They concluded that active sites for HER were present at the Mo-terminated edge. Conversely, H adsorption at both W- and S-terminated edges of WS_2 was close to thermoneutral.

Selenium is one period below sulfur in the chalcogenides, and consequently has similar chemical properties. A combination of these similarities and some important distinctions have generated significant interest in selenium containing materials for the HER. These distinctions include: (1) more pronounced metallic character with respect to sulfur, suggesting enhanced conductivity; (2) a larger ionic radius for Se,

and (3) lower ionization energy relative to S [7]. The high lying *p* state of the anion in these non-oxide materials, where the energy of the n*p* states is in the order O 2p < S 3p < Se 4p means that materials with S and Se show a more metallic character compared to oxides and this is important for promoting the optimum adsorption free energy of hydrogen.

A DFT study of the active sites of $MoSe_2$ and WSe_2 showed that, similar to their sulfide analogues, the basal planes of these materials are inert, with the active sites being present along the edges [47]. Some results from this work are included in table 1. A systematic computational study of layered TMDs of the form MX_2 (M = Ti, V, Nb, Ta, Mo, W, Pd, Pt; X = S, Se) identified some key trends with implications for practical implementation of such materials as HER catalysts [48]. The authors assessed the HER activity and stability of these materials based on computed values of ΔG_H and ΔG_{HX}, respectively. The latter quantity is the free energy of HX adsorption and an inverse relationship exists between H and HX binding. This implies that optimizing the HER activity can have detrimental effects on the stability of the catalyst. The authors considered ranges of chalcogen and hydrogen coverages, which can vary in a real system depending on the operating conditions. In general, hydrogen binding weakened with increasing hydrogen coverage. Moreover, through nudged elastic band (NEB) calculations, the authors concluded that the Volmer–Heyrovsky pathway is most likely for these materials, as prohibitively high activation barriers impede the Tafel step.

A study comparing the catalytic performance of electrodes consisting of porous arrays of MX_2 nanosheets (M = Mo, W; X = S, Se, Te), found a clear hierarchy in activity, following: selenides > sulfides > tellurides. $MoSe_2$ out-performed all other materials, which was attributed, in part, to a low Tafel slope of 77 mV dec^{-1}. The authors also postulated that diselenide sites have a higher intrinsic activity relative to equivalent disulfide and ditelluride sites.

Common among these studies that aim to use computational methods and experiment, to determine the origin of the activity of TMDs, is the identification of edges as active sites [49–51]. Computationally, this conclusion is drawn from the comparison of ΔG_H for edge and basal sites. In one experiment, samples of MoS_2 nanoparticles of different sizes on Au(111) were prepared and the electrocatalytic activity correlated linearly with the number of MoS_2 edge sites [51].

Bentley and colleagues implemented SECCM to create spatially resolved measurements of the HER activity at basal and edge sites of bulk MoS_2 [32]. Combining SECCM data with topographical information from scanning electron microscopy (SEM) and atomic force microscopy (AFM), showed enhanced activity at defects, steps, and crevices. The authors followed up this study with additional measurements of HER at MoS_2, with improved temporal and spatial resolution [33]. The results indicated a uniform activity in the basal plane and that the enhanced activity at the edges scaled with the step height.

These results indicate the necessity to engineer TMD-based catalysts that maximize the exposure of edge sites. However, strategies also exist for activating the basal plane. These and other considerations will be discussed in what follows.

3.1. Engineering edge sites

Nanoparticles are characterized by a high specific surface area and an abundance of low-coordinated surface sites and therefore, nanostructuring of TMDs is an approach to enhance the HER activity. TMDs consist of 2D layers that interact via van der Waals forces and various methods exist for exfoliating these layers to produce nanosheets or nanoflakes [52–54]. One such method involves applying adhesive tape to bulk TMD to peel off layers before transfer to a substrate material. This mechanical exfoliation technique was first employed by Novoselov and colleagues to isolate 2D single layers of graphene [55]. This method has since been used to deposit single- and few-layer nanosheets of TMDs onto SiO_2 coated Si substrates [56]. Another technique, described as similar to 'drawing chalk on a blackboard', was employed by Novoselov *et al* to transfer single layers of BN, graphite, and TMDs to an oxidized silicon wafer [57]. While this approach is low-cost, it does not afford precise control or uniformity of the exfoliated layers and is further hindered by a low yield.

Exfoliation of TMDs has also been achieved by irradiation with a high-power femtosecond laser [58]. The resulting flakes were a few layers thick with feature sizes of 100–200 nm, see figure 4.

Exfoliation of layers from bulk materials can also be achieved by various methods applied to suspensions of bulk powders in solvents [52, 53, 61]. These techniques include sonication, whereby the crystals suspended in an appropriate solvent are broken apart by exposure to ultrasonic waves. This approach has been used successfully to isolate flakes of layered materials such as TMDs and BN [62]. Sonication can be combined with intercalation, wherein molecules or ionic species are incorporated into the space between layers, weakening interlayer interaction and increasing layer spacing.

The preceding methods are examples of top-down techniques, beginning from bulk materials and deconstructing them by one means or another to obtain nanostructures. Bottom-up strategies involve building layers of materials on a substrate from their constituent parts. Chemical vapor deposition (CVD) is

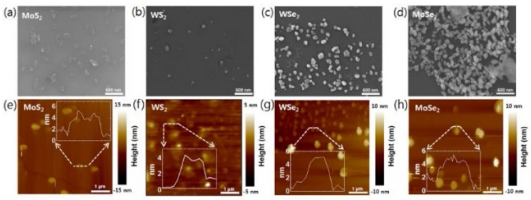

Figure 4. Laser exfoliated, few-layer nanosheets of (a), (e) MoS_2, (b), (f) WS_2, (c), (g) WSe_2, and (d), (h) $MoSe_2$ on SiO_2/Si substrate. SEM and AFM images are shown in the top and bottom panels, respectively. Reproduced with permission from [58].

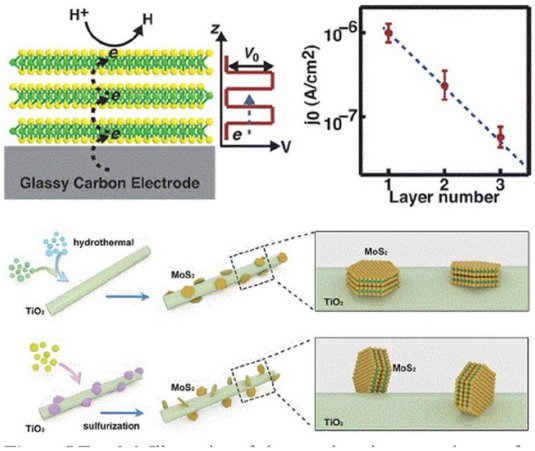

Figure 5. Top-left Illustration of electrons hopping across layers of a TMD and the potential barriers in the interlayer gap that must be overcome. **Top-right** The exchange current density of the MoS_2 film as a function of the layer number. Reproduced with permission from [59], © 2004 American Chemical Society. **Bottom** Schematic illustration of two methods of preparation of MoS_2/TiO_2 composites. The first is a hydrothermal method where the basal planes of the MoS_2 nanoplates lie flat on the TiO_2 surface. The second method involves CVD followed by sulfurization to achieve a configuration in which the MoS_2 nanoplates contact with TiO_2 surface along conductive edge planes. Reproduced with permission from [60], © 2016 WILEY-VCH Verlag GmbH & Co. KGaA, Weinheim.

an example of a bottom-up technique. In CVD, a heated substrate is exposed to volatile chemical precursors that react to deposit a layer of desired material. Tuning of operational parameters, such as temperature, the composition of the substrate and precursors, allows for control of the topography of the deposited material [63]. Nanotubes and fullerene-like nanoparticles of MoS_2 were obtained via reacting MoO_3 and S in an argon atmosphere [64].

Dendritic monolayers of MoS_2 were deposited on $SrTiO_3$ and subsequently transferred intact to Au foil [65]. The fractal-like geometry of these samples expose a wealth of active sites for HER and Tafel slopes of 73–85 mV dec^{-1} were reported. This compares favorably with values of 140–145 mV dec^{-1} measured for multi-layer MoS_2 grown on glassy carbon electrodes. The authors reported exchange current densities of 5–25 μA cm^{-2}, depending on preparation temperature, and durability tests showed a reproducible polarization plot after 1000 voltammetry cycles. Shi and coworkers deposited hexagonal TaS_2 flakes on Au foil via CVD [66]. The authors measured Tafel slopes in the range 33–42 mV dec^{-1} for 2H-TaS_2/Au samples, which compare with 31 mV dec^{-1} for Pt. The overpotentials, η_{10}, of the 2H-TaS_2 samples were between 65 and 150 mV and the exchange current densities were 100–179 μA cm^{-2}.

Hydrothermal and solvothermal synthesis are other bottom-up techniques, which for TMDs, typically involve the reaction of transition metal salts in aqueous/organic solutions at moderate to high temperatures (80 °C–240 °C) [52, 67, 68]. These methods allow for considerable control over the product by tuning preparation parameters, and morphologies such as nanorods, nanosheets, and nanoflowers of MoS_2 have been achieved in this way [67]. Such techniques have been used to grow MoS_2 on TiO_2 [69, 70] and carbon [71] nanotubes and reduced graphene oxide (rGO) [72]. Tafel slopes of 42 and 38 mV dec^{-1} and η_{10} of 98 and 95 mV were measured for MoS_2 grown on TiO_2 and Si doped TiO_2 nanotubes, respectively [69]. Li and colleagues measured a slope of 41 mV dec^{-1} for MoS_2 on rGO [72]. The value for η_{10} was ~150 mV and durability tests indicated negligible losses in HER current after 1000 cycles.

These are but a few of the techniques which have been implemented to deposit nanostructured TMDs on substrates and a comprehensive overview of other methods is provided in ref. [52]. A common feature of

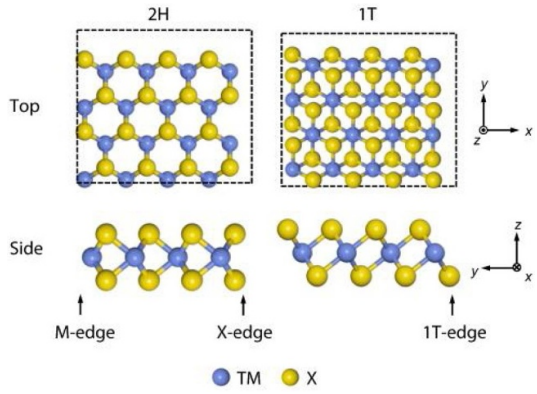

Figure 6. Unit cells for the basal plane of 2H and 1T TMD structures, showing the top and side views. Three types of edges, the 1T edge, the 2H M-edge, and the 2H X-edge are indicated by the arrows. Reproduced with permission from [48], © 2015 Elsevier.

these techniques is that the nanostructured TMD lies flat on the substrate surface[7, 59, 60] which minimizes the surface energy [73]. One consequence is that this orientation exposes the inactive basal plane. Secondly, electrons must transfer from the substrate to the active sites of the outermost layer, and in doing so, overcome the interlayer potential barrier; see top panels in figure 5.

He and coworkers addressed this issue by constructing edge-on MoS_2/TiO_2 heterostructures [60]. This was achieved in a two-step process wherein a hydrothermal preparation of MoO_2 on TiO_2 was followed by sulfurization by CVD and a schematic of this process is shown in the bottom half of figure 5. The core idea of this approach is that sulfurization is faster parallel to the basal plane, owing to the weak inter-layer interaction. A similar effect was achieved for MoS_2 on a carbon fiber paper (CFP) substrate by Hu *et al* using a microwave hydrothermal method [74]. By altering the reaction time, the researchers could control whether the exposed edges of MoS_2 were stepped or flat with respect to each other. The authors measured Tafel slopes of 121, 69, and 59 mV dec^{-1} for samples with randomly oriented, flat edged, and stepped edge MoS_2, indicating that stepped edges promote HER activity. Stepped edge samples required η_{10} of 104 mV and exhibited an exchange current density of 200 μA cm^{-2}. The cathodic overpotential to maintain 10 mA cm^{-2} decreased from 104 to 95 mV after 24 h, indicating good stability for the stepped edge MoS_2 catalyst.

CoS_2 was the subject of a combined theoretical and experimental study [75]. The group reported on the controlled fabrication of hierarchically mesoporous CoS_2 microspheres on CFP. The microspheres are terminated by vertical arrays of CoS_2 sheets with an abundance of exposed sulfur sites. The authors reported a Tafel slope of 67 mV dec^{-1} and a low overpotential of 90 mV at 10 mA cm^{-2}. DFT analysis of free energies of hydrogen adsorption at different CoS_2 facets, at a coverage of 1/8, monolayer showed computed values for ΔG_H in the range 0.04–0.06 eV.

Wang *et al* reported Tafel slopes of 60 and 77 mV dec^{-1} for $MoSe_2$ and WSe_2 films grown vertically on a CFP substrate [73]. The authors concluded that the curvature and roughness of the substrate enhanced the exposure of active sites. This lead to values for η_{10} of 250 and 300 mV for $MoSe_2$ and WSe_2 on CFP, respectively. Moreover, the performance of both catalysts improved slightly after 15 000 cycles at 50 mV s^{-1}.

3.2. Activating the basal plane

Before describing approaches to increasing the activity of basal plane of TMDs we first note that these materials exist predominantly in two polymorphs, denoted 2H and 1T. The 2H phase exhibits tetrahedral coordination while the 1T phase is characterized by octahedral coordination, as shown in figure 6. For bulk group 6 TMDs, such as MoS_2 and WS_2, the 2H phase is thermodynamically favored over the metastable 1T phase, although this is not true for all TMDs [48]. The electronic properties of these materials depend on the structural geometry. For example, the basal plane of MoS_2 is semiconducting in the 2H phase and becomes metallic in the 1T phase. In addition to enhanced conductivity, the 1T phase has active sites for HER in the basal plane [7, 48, 76, 77]. This was deduced from measurements of the activities of 2H- and 1T-MoS_2 samples after oxidation; the activity of 2H-MoS_2 decreased after oxidation of edge sites whereas the activity of 1T-MoS_2 was undiminished, implying the presence of active sites in the basal plane.

This suggests a strategy for promoting the activity of TMDs might be to promote their metallic phase. The 2H-1T phase transition has been shown to occur in samples of MoS_2 upon exfoliation *via* Li intercalation [16, 76, 77]. Tafel slopes of 40 [76] and 43 [77] mV dec^{-1} were measured for 1T-MoS_2 samples prepared in this manner. As mentioned above, metallic 2H-TaS_2 deposited on Au foil (Tafel slopes: 33–42 mV dec^{-1}) showed HER activity comparable to that of Pt (31 mV dec^{-1}) [66], and similar results were found for

1T-MoS_2 decorating TiO_2 nanotubes (38–42 mV dec^{-1}) [69]. Voiry and colleagues also used Li intercalation to isolate metallic 1T-WS_2 and obtained a Tafel slope of 60 mV dec^{-1}, compared with 110 mV dec^{-1} for 2H-WS_2 [79]. Durability tests entailed 10 000 cycles and monitoring of current density over 100 h of continuous operation at −0.3 V and the results indicated a stable performance with no loss of 1T phase.

Using hydrothermal synthesis and varying the temperature and the ratio of reactants, Yin and coworkers isolated 1T-$MoSe_2$ nanosheets for which they measured a Tafel slope of 52 mV dec^{-1} and η_{10} of 152 mV [80]. Formation of 1T phase was achieved during synthesis with a large excess of the $NaBH_4$ reductant. The catalyst stability was assessed by cycling the electrodes 1000 times, which showed negligible losses in current density. Kong and coworkers produced a nanoparticulate $CoSe_2$ film on CFP via selenization of a cobalt oxide layer with Se vapor [81]. The resulting electrode consisted of $CoSe_2$ nanoparticles with dimensions of tens of nanometers. X-ray diffraction (XRD) analysis revealed the presence of predominantly cubic pyrite phase with some evidence of marcasite and amorphous phases. The metallic property of $CoSe_2$ contributed to the high HER activity, as shown by a Tafel slope of 40 mV dec^{-1} and η_{10} of 137 mV. At an overpotential of 155 mV, the current density remained stable at ∼20 mA cm^{-2} for over 60 h.

It is also possible to activate the basal plane of semiconducting 2H-MoS_2. This was first achieved by Li and colleagues through combinations of S-vacancies and strain, see figure 7 [82]. 2H-MoS_2 flakes were grown by CVD on a Si/SiO_2 wafer before transfer to a gold substrate and S-vacancies were introduced by exposure to argon plasma. The combination of S-vacancies and strain could be tuned such that the optimal condition of $\Delta G_H = 0$eV was satisfied. The authors identified S-vacancies as active sites and DFT calculations revealed defect gap states that could be shifted toward the Fermi level by application of strain, which would promote the adsorption of hydrogen. Experimentally, this manifested as measured Tafel slopes of 60 mV dec^{-1} for the strained sample with S-vacancies; a value of 98 mV dec^{-1} was measured for the sample without strain or vacancies.

The role of gap states in the HER activity was also investigated by Li and coworkers in their study of MoS_2 films grown on a Mo substrate[83]. A combination of S-vacancies and Pt-doping introduces gap states, which promote the HER activity. The authors reported a Tafel slope of 38 mV dec^{-1} for the Pt/MoS_2/Mo heterostructure, which is compared with 68 mV dec^{-1} for MoS_2/Mo. Values for η_{10} of 58 and 198 mV were recorded for Pt/MoS_2/Mo and MoS_2/Mo, respectively, further highlighting a crucial role for Pt in the catalytic activity. Moreover, the authors found no decrease in activities after 1000 CV cycles.

A comprehensive study of active sites of MoS_2 reported a maximum in catalytic activity for S-vacancy concentrations in the range of 7%–10% [84]. The crystalline quality near the vacancy also strongly affected the activity of the vacancy. Dong and colleagues described morphological control of MoS_2 flakes prepared via CVD, and as a consequence of this method, control of the abundance of S-vacancies [85]. The authors reported enhanced HER activity for hexagonal MoS_2 flakes on glassy carbon with a Tafel slope of 53 mV dec^{-1}; the hexagonal samples also exhibited an exchange current density of 91 μA cm^{-2} and η_{10} of 104 mV. After a slight improvement in performance after 3000 cycles, the performance remained stable from 3000 to 6000 cycles. S-vacancies have also been introduced to the basal plane of MoS_2 by electrochemical desulfurization as a viable alternative to Ar plasma exposure [86]. Desulfurization decreased the Tafel slopes from 151 to 102 mV dec^{-1} (after iR correction). Stability was assessed over 8 h, over which the current remained the stable.

Gao *et al* reported a method for heterostructuring defect-rich MoS_2 nanoflakes on exfoliated MoS_2/WS_2 scaffolds, via a hydrothermal approach [87] and measured Tafel slopes of 81 and 73 mV dec^{-1} for the flakes on MoS_2 and WS_2, respectively. There was negligible variation in polarization curves after 3000 cycles. Geng and colleagues approached activating the basal plane by fabricating porous MoS_2 [88]. This was achieved by preparing Al-doped MoS_2, followed by submersion in NaOH solution to remove Al. The resulting porous MoS_2 yielded a Tafel slope of 62 mV dec^{-1}. The measured η_{10} was 201 mV and no differences were observed in polarization curves before and after 3000 CV cycles. A systematic study of the impact of phase, edge sites and S-vacancies on the HER activity concluded that phase is the major determining factor [89]. The 1T-MoS_2 samples consistently outperformed the 2H phase. Mesoporous 1T-MoS_2, prepared via liquid-ammonia-assisted lithiation and with an abundance of S-vacancies yielded the best activity with a Tafel slope of 43 mV dec^{-1} and η_{10} of 154 mV. The current density yielded by this sample decreased by <7% after 1000 cycles.

3.3. Amorphous TMDs

Amorphous MoS_x has also been investigated as a HER catalyst, with reports of activities rivalling those of 1T-MoS_2 [90, 91]. One advantage of amorphous MoS_x is the ease and economy with which it can be synthesized; simple, wet chemical techniques, requiring no high-temperature processing, have been reported in the literature [92, 93]. Merki *et al* prepared amorphous MoS_2 films using electro-polymerization

procedures and reported high current densities at low overpotentials with a Tafel slope of 40 mV dec^{-1} and η_{15} of 200 mV [90].

A study by Wu and colleagues attributed the high activity of amorphous MoS_2 to similarities with 1T-MoS_2 in terms of bonding character and electronic structure [91]. The authors identified a short Mo–Mo bond, common to 1T-phase and amorphous samples, as a crucial feature for the HER activity. Tafel slopes of 65, 58, and 42 mV dec^{-1} were measured for 2H, 1T- and amorphous MoS_2, respectively. Wang *et al* fabricated copolymer hybrid films consisting of polypyrrole and amorphous MoS_x ($x \sim 5$) [94]. This was achieved via electrochemical copolymerization of pyrrole and $(NH_4)_2MoS_4$ and the result exhibited a HER activity comparable to that of commercial Pt/C catalysts with a Tafel slope of 29 mV dec^{-1}; however, a clear decrease in current was observed after 5000 s at a potential of −0.05 V (vs. RHE).

A strategy to further enhance the HER activity of amorphous MoS_x via doping with first row transition metals was investigated by Merki *et al* [95]. The Tafel slopes for all samples of M-MoS_3 (M=Mn, Fe, Co, Ni, Cu, Zn) were in the range 39–43 mV dec^{-1}. The authors found that Fe-, Co-, and Ni-doping promoted growth of the MoS_3 film, resulting in higher surface area and catalyst loading, and consequently, enhanced HER activity. However, the authors also concluded that the improved activity was not attributable solely to morphological effects and that the dopants increased the intrinsic catalytic activity. The impact on activity was pH-dependent, with Fe- and Co-doping performing best under acidic and neutral conditions, respectively.

The use of MoS_x-coated carbon electrodes in microbial electrolysis cells (MECs) under operating conditions was investigated by Kokko and colleagues [96]. MECs can renewably produce H_2 while simultaneously treating wastewater. Three different carbon supports were considered: activated carbon cloth, electrospun carbon, and buckypaper (BP); in combination with three deposition methods: electrodeposition, drop coating, and impregnation followed by heat treatment. The best performing MoS_x electrodes exhibited onset potentials only slightly higher than that of a platinum electrode and Tafel slopes were in the range of 40–100 mV dec^{-1}. The values for η_{10} were in the range 130–250 mV. Importantly, the catalytic efficiency improved over time whereas the Pt electrode was slowly deactivated. This latter result is common for amorphous MoS_x electrodes and is attributed to structural changes induced under HER conditions.

Amorphous $MoSe_x$ has also been reported as an efficient catalyst for the HER [97]. To obtain amorphous $MoSe_3$, Nguyen *et al* employed the same strategy as described by Benck and coworkers to prepare MoS_3 [93]. While the as-prepared amorphous $MoSe_3$ nanopowder was inactive, exposure to HER conditions rendered the catalyst active. This was attributed to the development of structures with composition close to that of $MoSe_2$. The active catalytic material was more robust than its MoS_x analogue and operated in a wider range of pH solutions. In a pH 0 electrolyte $MoSe_x$ displayed a Tafel slope of 60 mV dec^{-1} and η_{10} of 270 mV.

Amorphous $CoSe_x$ films were deposited electrochemically onto planar Ti supports under ambient conditions [98]. The films were mesoporous with pore sizes estimated to be ∼20 nm in diameter and exhibited a Tafel slope of 60 mV dec^{-1} and η_{10} of 135 mV. The catalyst performance remained stable after >16 h of operation at -10 mA cm^{-2}.

3.4. Heterostructuring

Heterostructuring consists of interfacing two or more materials of different composition or phase. In this way, it is possible to combine the qualities of each phase and moreover, capitalize on novel properties which emerge at the interface.

Wang and coworkers grew MoS_2 on CoS_2 decorated carbon cloth (MoS_2/CoS_2/CC) and investigated the activity of this sandwich-structured electrode for HER [99]. The CoS_2 was deposited on the carbon cloth (CC) electrochemically prior to growth of MoS_2 via a hydrothermal method. The interplay between the MoS_2 and CoS_2 phases was shown to play a crucial role in both the HER activity and stability of the electrode. This was established by comparing the performance of MoS_2/CoS_2/CC, MoS_2/CC, and CoS_2/CC, for which Tafel slopes of 37, 50, and 60 mV dec^{-1} were measured, respectively. MoS_2/CoS_2/CC exhibited η_{10} of 118 mV and showed no decay in performance after 4000 CV cycles. Further stability tests, conducted via continuous HER at a constant overpotential, indicated a decrease in activity to 80% of the initial current density in the first 60 h, after which the activity plateaued and remained at 80% up to 83 h. The enhanced activity was attributed to optimal adsorption of hydrogen at interfacial S-sites; strong bonding interactions between MoS_2 and CoS_2 were the origin of the superior stability, compared to the individual materials.

In their 2016 paper [100], Staszak-Jirkovský and colleagues established that, while amorphous CoS_x is more active than amorphous MoS_x, as measured by HER activity in acidic and alkaline media, the latter is more stable, and this observation informed the rational design of a low-cost $CoMoS_x$ chalcogel catalyst. The resulting catalyst consisted of Mo_3S_{13} clusters interconnected by CoS_8 octahedra capped by polysulfide oligomers in a compact structure and was highly active and stable, irrespective of pH. In alkaline media there was a large difference in activity, following: $MoS_x \ll CoMoS_x \ll CoS_x$; whereas, in acid solutions the

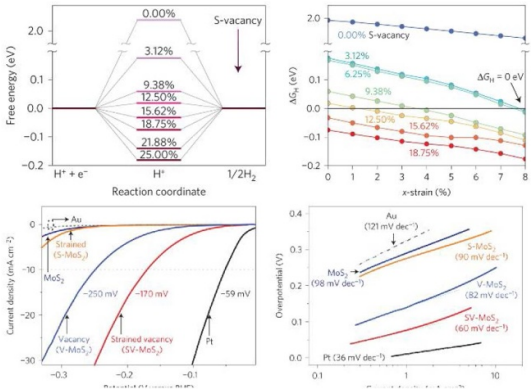

Figure 7. Free energies of HER at the MoS_2 basal plane, computed for the S-vacancy range of 0–25%. (**b**) ΔG_H vs. %x-strain for the S-vacancy range of 0–18.75%. The black line indicates combinations of S-vacancy and strain that yield the optimal $\Delta G_H = 0$ eV. (**c**) Linear sweep curves for the Au substrate; Pt electrode; unstrained and vacancy-free MoS_2, (MoS_2); strained [∼1.35%] MoS_2 without S-vacancies, (S-MoS_2); unstrained MoS_2 with S-vacancies [∼12.5%] (V-MoS_2); and strained [∼1.35%] MoS_2 with S-vacancies [∼12.5%] (SV-MoS_2). (**d**) Tafel plots corresponding to the linear sweep curves in (**c**). Reproduced with permission from [82] © 2015, Springer Nature.

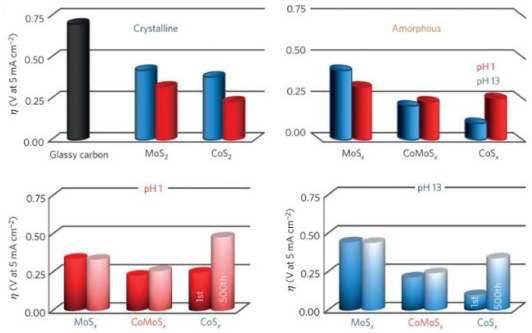

Figure 8. (**a**) Overpotentials required for 5 mA cm^{-2} current densities, η_5, in pH 1 and pH 13, for both crystalline and amorphous TMS_x. Crystalline CoS_2 is always more active than MoS_2, and both materials are more active in acidic than alkaline solutions. For amorphous samples, CoS_x is always more active, particularly in alkaline solution. The activity of $CoMoS_x$ is almost independent of pH. (**b**) Overpotentials, η_5, in pH 1 and pH 13, before and after 500 CV cycles. CoS_x is the most active and least stable material. The $CoMoS_x$ chalcogen is stable and active, and shown as a pH-universal catalyst for the HER. Reproduced with permission from ref. [100] © 2015, Springer Nature.

differences were less significant, with $MoS_x < CoS_x \leq CoMoS_x$, as shown in figure 8. Moreover, the authors noted that less active crystalline MoS_2 and CoS_2 were more stable than their amorphous analogues by a factor of 10, which implies an important role for the density of defects in the relationship between activity and stability.

Zhang and coworkers prepared polymorphic $CoSe_2$ with mixed orthorhombic and cubic phases by calcining amorphous $CoSe_x$, fabricated by electrodeposition [101]. The authors described polymorphic $CoSe_2$ (p-CoSe2) as a highly active HER catalyst with activities exceeding those of amorphous CoS_x, cubic $CoSe_2$ and CoSe. The phase and morphology of the samples were tuned via the calcination temperature. At 300 °C the sample presented as mixed orthorhombic and cubic phases. Calcination at 450 °C and 600 °C produced cubic $CoSe_2$ (c-$CoSe_2$) and CoSe, respectively. The measured Tafel slopes were 38, 31, 39, and 55 mV dec^{-1} for $CoSe_x$, p-$CoSe_2$, c-$CoSe_2$, and CoSe, respectively. The corresponding values for η_{10} were 180, 150, 200, and 270 mV, indicating that the polymorphic sample had the best activity. The value of η_{10} was found to increase by 8 mV for p-$CoSe_2$ after 40 h of galvanostatic measurement.

3.5. Ternary TMDs

Ternary TMDs (TTMDs) have also been considered in the pursuit for active and stable HER catalysts [102]. TTMDs have the general formula $M^1_zM^2_{1-z}X_2$ or $MX^1_{2z}X^2_{2(1-z)}$, where M^1, M^2 and M are transition metals ($M^1 \neq M^2$) and X^1, X^2 and X = S, Se or Te ($X^1 \neq X^2$). The properties of TTMDs can be tuned by altering the composition and the molar ratio, *z*.

Kiran and coworkers found that $MoS_{2z}Se_{2(1-z)}$ alloys possessed higher HER activity compared to MoS_2 and $MoSe_2$ [103]. The authors systematically studied the structure–activity relationship by varying the composition and found that MoS_1Se_1 presented the highest HER activity among the catalysts under study.

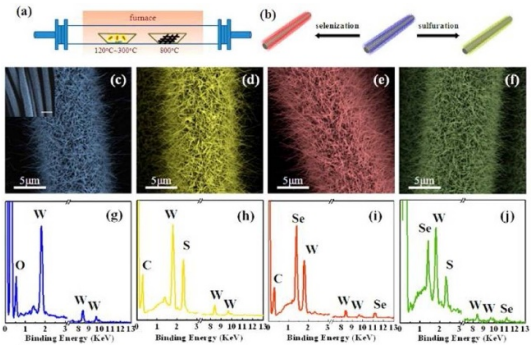

Figure 9. (**a**) and (**b**) Schematics of the experimental setup for fabrication of WS_2, WSe_2, and $WS_{2(1-x)}Se_{2x}$ nanotubes. SEM images of (**c**) WO_3 nanowires and (**d**) WS_2, (**e**) WSe_2, and (**f**) $WS_{2(1-x)}Se_{2x}$ nanotubes. X-ray energy dispersive spectroscopy (EDS) pattern of (**g**) WO_3 NWs and (**h**) WS_2, (**i**) WSe_2, and (**j**) $WS_{2(1-x)}Se_{2x}$ NTs. Reproduced with permission from [106] © (2014) American Chemical Society.

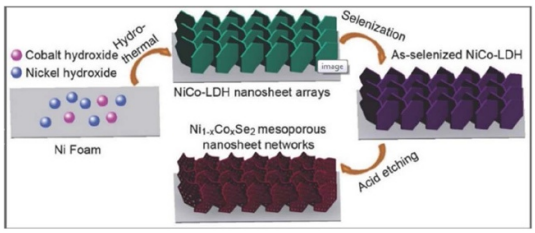

Figure 10. Schematic showing the process for fabrication of mesoporous $Ni_{(1z)}Co_zSe_2$ nanosheets. Reproduced with permission from [78] © 2017 WILEY-VCH Verlag GmbH & Co. KGaA, Weinheim.

The alloys were prepared via a high temperature solid-state reaction technique followed by exfoliation to obtain catalysts of a few layers. The authors measured Tafel slopes in the range 50–60 mV dec^{-1}, compared to 96 and 95 mV dec^{-1} for MoS_2 and $MoSe_2$, respectively, and attributed the higher activity of MoSSe to improved electronic conductivity. Exchange current densities, j_0, of 320, 36, and 45 μA cm^{-2} were measured for samples of MoS_1Se_1, MoS_2, and $MoSe_2$, indicating facile HER kinetics for the TTMD, for which negligible differences were found in the performance after 1000 cycles.

Konkena *et al* studied MoSSe interfaced with rGO [104]. The composite catalyst was constructed *via* self-assembly, owing to the electrostatic attraction between the oppositely charged nanosheets. The authors reported that the nanocomposite heterostructures were active and stable electrocatalysts for HER. They measured a Tafel slope of 51 mV dec^{-1} and η_{10} of 155 mV. Stability tests showed no decrease in performance after 5000 cycles.

Liu *et al* grew $CoS_{2z}Se_{2(1-z)}$ ($z = 0.67$) nanowires on flexible carbon fiber [105]. This composite material exhibited high catalytic activity and stability. A Tafel slope of 44 mV dec^{-1} for $CoS_{2z}Se_{2(1-z)}$ compared with values of 69 and 46 mV dec^{-1} for CoS_2 and $CoSe_2$ nanowires, respectively. The authors measured η_{10} of 130 mV, with no decrease in activity after 1000 cycles. Xu *et al* synthesized high-quality WS_2 and WSe_2 nanotubes on carbon fibers via CVD, see figure 9 [106]. The authors also reported synthesis of $WS_{2z}Se_{2(1-z)}$ with systematic control of the S/Se ratio through optimization of growth conditions. The WS_2, WSe_2, and $WS_{2z}Se_{2(1-z)}$ ($z = 0.48$) nanotubes exhibited Tafel slopes of 113, 99, and 105 mV dec^{-1} and values for j_0 of 12, 3, and 29 μA cm^{-2}. The enhanced activity of these TTMD catalysts is due to improved conductivity, which results from incorporation of Se into the WS_2 lattice, as evidenced by analyses of the electronic structure.

Zhang and colleagues implemented CVD techniques to grow dendritic $WS_{2z}Se_{2(1-z)}$ flakes on a $SrTiO_3$ substrate by sulfurization and selenization of WO_3 powder [107]. The flakes, with a morphology that produces an abundance of active edge sites, were transferred to Au foil to measure their HER capability. The $WS_{2z}Se_{2(1-z)}$ on Au electrode, with an S to Se ratio of 19 to1, presented a Tafel slope and η_{10} of 67 mV dec^{-1} and 156 mV which were lower than those measured for dendritic WS_2 (87 mV dec^{-1} and 310 mV). Moreover, the TTMD catalyst exhibited excellent stability, with negligible decay in performance after 1000 cycles. Other studies of $WS_{2z}Se_{2(1-z)}$ inferred that active sites are present on the basal plane of the TTMD due to lattice strain arising from the different atomic radii of S and Se atoms [108, 109].

Xia *et al* prepared $Ni_zCo_{(1-z)}Se_2$ ($z = 0.33$) solid solutions by selenization of a nickel cobalt precursor [110]. The resulting $Ni_zCo_{(1-z)}Se_2$ catalyst consisted of mixed cubic and orthorhombic phases. Through temperature dependent measurements of the conductivity, the authors described the metallic-like electrical

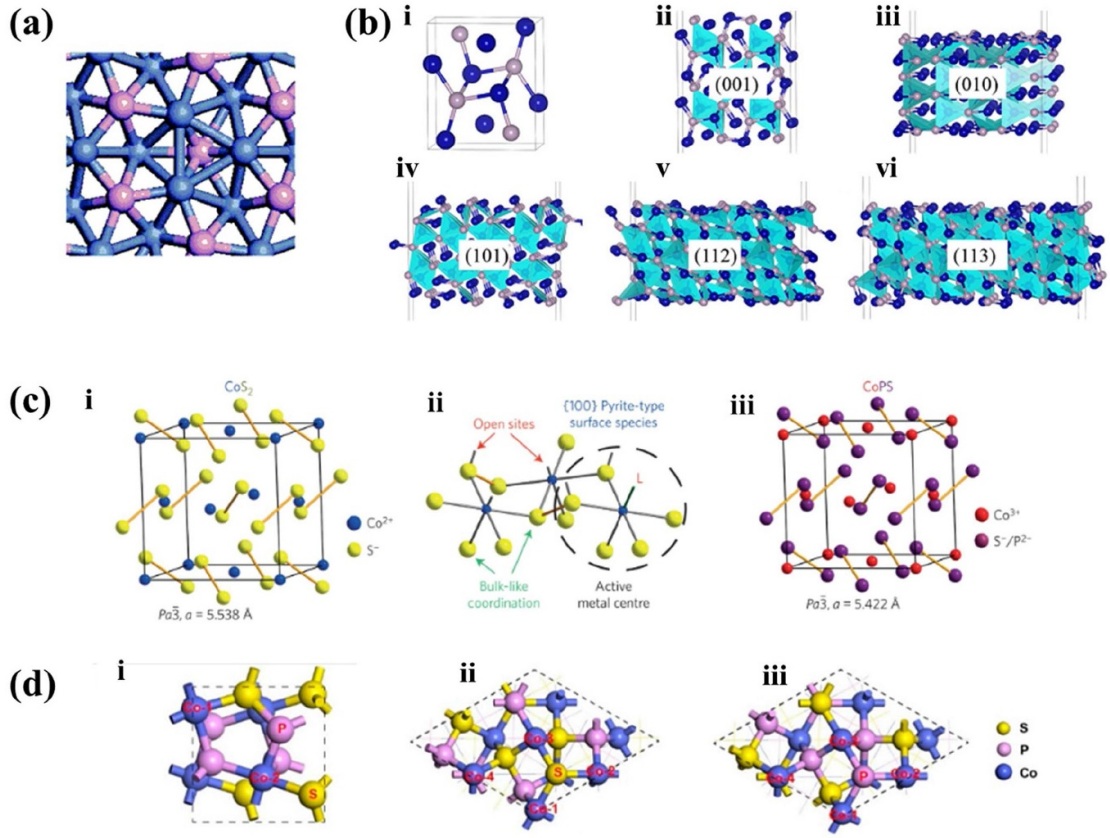

Figure 11. (**a**) Structure of Ni_2P (001) surface with Ni represented by navy and P by purple. Reproduced with permission from [115], © (2005) American Chemical Society. (**b**) Structures of (**i**) the unit cell, (**ii**) the (001) facet, (**iii**) the (010) facet, (**iv**) the (101) facet, (**v**) the (112) facet, and (**vi**) the 113 facet of Co_2P. Co is represented by blue and P by pink. Reproduced with permission from [116] © 2019 Wiley-VCH Verlag GmbH & Co. KGaA, Weinheim. (**c**) Structures of (**i**) cobalt pyrite CoS_2, (**ii**) the (001) pyrite surface coordination environment, and (**iii**) the pyrite-type cobalt phosphosulfide (CoPS). Reproduced with permission from [117] © 2015, Springer Nature. (**d**) Top views of (**i**) CoPS (100), (**ii**) S-terminated, and (**iii**) P-terminated CoPS (111). Reproduced with permission from ref. [118], © (2018) American Chemical Society.

conductivity of the TTMD solid solution. The room-temperature conductivity of $Ni_zCo_{(1-z)}Se_2$ was three times that of $CoSe_2$. DFT calculations indicated that incorporation of Ni into the $CoSe_2$ lattice lowered the free energy of hydrogen adsorption at edge sites. $Ni_zCo_{(1-z)}Se_2$ operated under both acidic and alkaline conditions and measurements in an acidic electrolyte yielded a Tafel slope of 35 mV dec^{-1} and η_{10} of 65 mV, with no loss of performance after 24 h of electrolysis.

Lie *et al* prepared 3D $Ni_{(1-z)}Co_zSe_2$ mesoporous nanosheet networks with tunable stoichiometry ($z = 0$–0.35) which operated as HER catalysts with excellent stability over a wide pH range [78]. A schematic of the fabrication process is shown in figure 10. The TTMD samples were prepared on nickel foam and by varying the Ni:Co ratio the authors identified $Ni_{(1-z)}Co_zSe_2$ ($z = 0.11$) as the optimal configuration. DFT calculations revealed that $Ni_{0.89}Co_{0.11}Se_2$ was metallic with high electrical conductivity. The electronic structure that resulted from substitutional doping of Co into the $NiSe_2$ lattice led to favorable adsorption free energies of H and H_2O at the surface. This result indicated that $Ni_{0.89}Co_{0.11}Se_2$ could operate with high HER activity in all pH environments. Tafel slopes of 0.39, 0.78, and 0.52 mV dec^{-1} were measured for $Ni_{0.89}Co_{0.11}Se_2$ operating in acidic, neutral, and alkaline conditions, respectively. The corresponding values for η_{10} were 52, 82, and 85 mV. Performance data for selected sulfur- and selenium-based HER catalysts are presented in tables 2 and 3, respectively, which can be found at the end of this review.

4. Metal phosphides

Metal Phosphides are another group of non-oxide materials that are seeing significant interest in HER. Similar to chalcogenide catalysts based on NiMo, Mo_2C and MoS_2, phosphide materials are HDS catalysts and are therefore potentially active for HER. Among phosphides, Ni_2P, CoP, Fe_2P, and MoP and ternaries have been studied as HDS catalysts [111–114].

Figure 11 shows the atomic structure of a range of metal phosphides, namely the Ni_2P (001) surface (figure 11(a)) Co_2P surface facets in figure 11(b), CoS_2 in figure 11(c), and CoSP in figure 11(d). These structures are taken from references [115–118].

4.1. Pure phosphorous materials

Phosphorous has been explored as a non-noble metal photocatalyst. Hu *et al* showed that fibrous phase red phosphorus functions as a semiconductor photocatalyst for visible-light-driven hydrogen evolution [122]. The fibrous phosphorus was prepared by loading onto photoinactive SiO_2 fibers or treating single phase fibrous phosphorous ultrasonically. Red P is useful as it is inexpensive and of low-toxicity and is more stable than Si in water under irradiation because it is not deactivated by surface oxidation. Fibrous P is a direct band gap semiconductor with a very high conduction band minimum of −0.9 V vs. NHE. This is higher than the theoretical potential of hydrogen evolution (0 V vs. NHE) and the previously reported values for Hittorf red P (−0.25 V) and Si (−0.2 to −0.35 V); this indicates that fibrous P is more favorable for water reduction than red P or Si.

The yield of hydrogen from photocatalytic water splitting was evaluated by using methanol as a sacrificial reagent and Pt as a cocatalyst. Hydrogen generation over time was evaluated at intervals of 1 h under visible light irradiation (wavelength > 420 nm). The resulting catalyst displayed steady hydrogen evolution rates of 633 and 684 μmol/g/h. These values are much higher than for amorphous P and Hittorf Phosphorous, for which H_2 evolution rates of 0.6 and 1.6 μmol/g/h were obtained.

Zhu *et al* prepared a binary nanohybrid composed of nanoflakes of black phosphorous interfaced with carbon nitride nanosheets (BP/CN) which was studied for H_2 evolution in the presence of methanol as a hole scavenger [123]. Trace amounts of H_2 were evolved using the single components. The optimum H_2 evolution for 1.5 mg of BP/CN reached 1.93 μmol for 3 h under >420 nm light irradiation without any metal elements. This catalyst also exhibited generation of H_2 (0.46 μmol) under >780 nm radiation for 3 h. The improvement in hydrogen evolution is proposed to arise from the strong interfacial interaction between BP and CN and the resulting efficient charge transfer at the interface that inhibits the recombination of photogenerated charges. The optimal ratio of BP:CN was 1:4, which resulted in a H_2 evolution rate of 427 μmol/g/h. The CN component is excited under visible light to generate electrons and holes in CN, while BP is an electron acceptor from the CN, which then inhibits the recombination of photogenerated charges in CN.

BP nanoflakes exhibit very broad absorption in UV to NIR region with an absorption edge around 1740 nm. CN nanosheets display a visible absorption edge around 463 nm, with a band gap of 2.7 eV. For the BP-CN heterostructure, the absorption edge for CN displays a slight red-shift to 470 nm. The heterostructure permits additional light absorption in the visible and NIR region.

Under simulated solar ($\sim$100 mW cm^{-2}) irradiation for 3 h, 8 mg of BP/CN produced 13.5 μmol of H_2, with a solar-to-hydrogen efficiency of *ca.* 1.51%.

Tian *et al* demonstrated that amorphous cobalt phosphide (CoP)-supported black phosphorus nanosheets exhibit robust hydrogen evolution from pure water (pH = 6.8), without bias [124]. The apparent quantum efficiency is 42.55% at 430 nm and the energy conversion efficiency is over 5.4% at 353 K. This was attributed to the extremely efficient utilization of solar energy ($\sim$75% of incident light) by black phosphorus nanosheets and the high-carrier separation efficiency induced by the interface with amorphous Co–P.

The H_2-evolution rate was assessed for 40 mg of catalyst dispersed in 150 ml. The as-prepared BP nanosheets yielded 1.2 μmol h^{-1} of H_2 and after supporting amorphous CoP nanoparticles (P:Co ratio of 3:1), the H_2-evolution rate increased to 15 μmol h^{-1}. This is due to the low recombination of electron–hole pairs induced by formation of the interface with the amorphous Co–P cocatalyst. The highest H_2-evolving activity was at a mass ratio of P:Co of 8:1; 40 mg of this catalyst produced 29.4 μmol h^{-1} of H_2. However, increasing the ratio of P to Co decreased activity due to a decrease in light absorption.

The catalyst showed high stability over 40 h activity under cycling and in a pH range from 2 to 13. The STH efficiency in this CoP/BP system was obtained *via* loading 40 mg of Co–P/BP catalyst in 150 ml pure water under AM1.5 G simulated sunlight illumination (100 mW cm^{-2}). After 2 h of irradiation, 160 umol of H2 was generated, giving an STH efficiency of 0.66% at room temperature. Activation energy for hydrogen evolution was 32.8 kJ mol^{-1}. This is smaller than from acidic or basic solutions.

4.2. Nickel phosphides

In 2005, early work from Liu and Rodriguez proposed that Ni_2P could be a practical catalyst for HER based on DFT calculations [115]. Their calculations on the (001) surface showed favorable H-binding together with the stability of a solid catalyst. They found that the Ni concentration was diluted by introduction of P elements, which made $Ni_2P(001)$ behave like hydrogenase rather than the pure metal surface. In the HER process, hydrogen binds strongly at Ni hollow sites, but with the inclusion of P, the hydrogen is less strongly bound so that H_2 could be removed from $Ni_2P(001)$ surface.

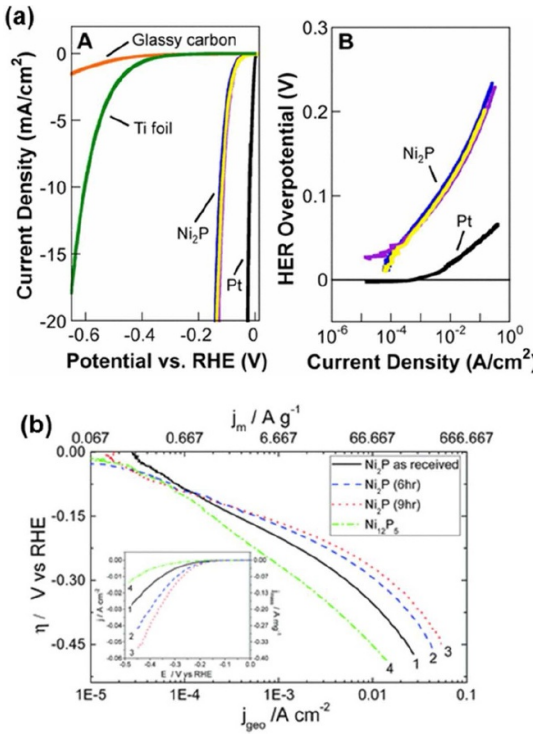

Figure 12. (**a**) Polarization curves for three individual Ni_2P electrodes, along with glassy carbon, Ti foil, and Pt (**A**) and the corresponding Tafel plots of Ni_2P and Pt (**B**). Adapted with permission from [125], © (2013) American Chemical Society.. (**b**) Steady state Tafel plot for the HER on Ni_2P samples with a metal phosphide loading of 150 μg cm^{-2}. Bottom axis gives the geometric current density and the top axis gives the mass-specific current density. Inset: raw data for the Tafel plot. Reproduced with permission from ref. [126].

Ni_2P nanoparticles were deposited onto a Ti foil substrate, which was followed by an annealing treatment [125]. The Ni_2P/Ti electrode exhibited excellent HER activity with an exchange current density of 33 μA cm^{-2} and a Tafel slope of ~46 mV dec^{-1}. Figure 12(a) shows a comparison of polarization curves for three individual Ni_2P electrodes, along with glassy carbon, Ti foil, and Pt. However, further work showed that the stability of electrode was not satisfactory.

Kucernak and Sundaram examined the interplay between activity and corrosion resistance for varying phosphorous content in NiP samples [126]. Metal rich phosphides show high electronic conductivity but suffer from reduced stability in acidic medium compared to phosphorus rich materials; so the key is to find a balance between the metal and phosphorous content while enhancing the HER activity.

Nickel phosphide alloys show higher corrosion resistance than pure Ni metal. There are three important aspects contributing to the corrosion resistance of these phosphides:

- Metal dissolution is thermodynamically less favorable in a metal alloy with phosphorus.
- Metal phosphides form amorphous films that are less susceptible to oxidation at grain boundaries.
- On oxidation, phosphorus oxidises to phosphate, which is much less soluble than other ionic species that can form during metal dissolution.

This work showed that nickel-based phosphides, namely Ni_2P and $Ni_{12}P_5$ with 33 and 29 at% P can be used for HER in an acidic medium. Ni_2P samples were prepared via ball-milling commercially purchased Ni_2P from 2–9 h and $Ni_{12}P_5$ was prepared hydrothermally. The corrosion behavior was examined in two overpotential regimes: low (0 to −140 mV) and high (−140 to −450 mV). The lower potential regime is more typical of practical HER conditions and under these conditions the possibility of metal corrosion is minimized due to the low electrochemical potential.

A higher phosphorus content produced higher HER activity, as measured by lower Tafel slopes and higher exchange current densities. The Tafel plots in figure 12(b) are shown for the as-received Ni_2P, Ni_2P after ball-milling for 6 and 9 h, and $Ni_{12}P_5$. In the low potential regime, the Ni_2P electrocatalysts showed Tafel slopes of 79–84 mV dec^{-1}, depending on the duration of ball milling, whereas a slope of 108 mV dec^{-1} was recorded for $Ni_{12}P_5$. Recognizing that suitable hydrogen evolution catalysts should show low corrosion current densities but high exchange current densities, the results of this work showed that Ni_2P samples ball-milled for 6 h best met this demand. Although initially highly active, the Ni_2P catalysts displayed a decay

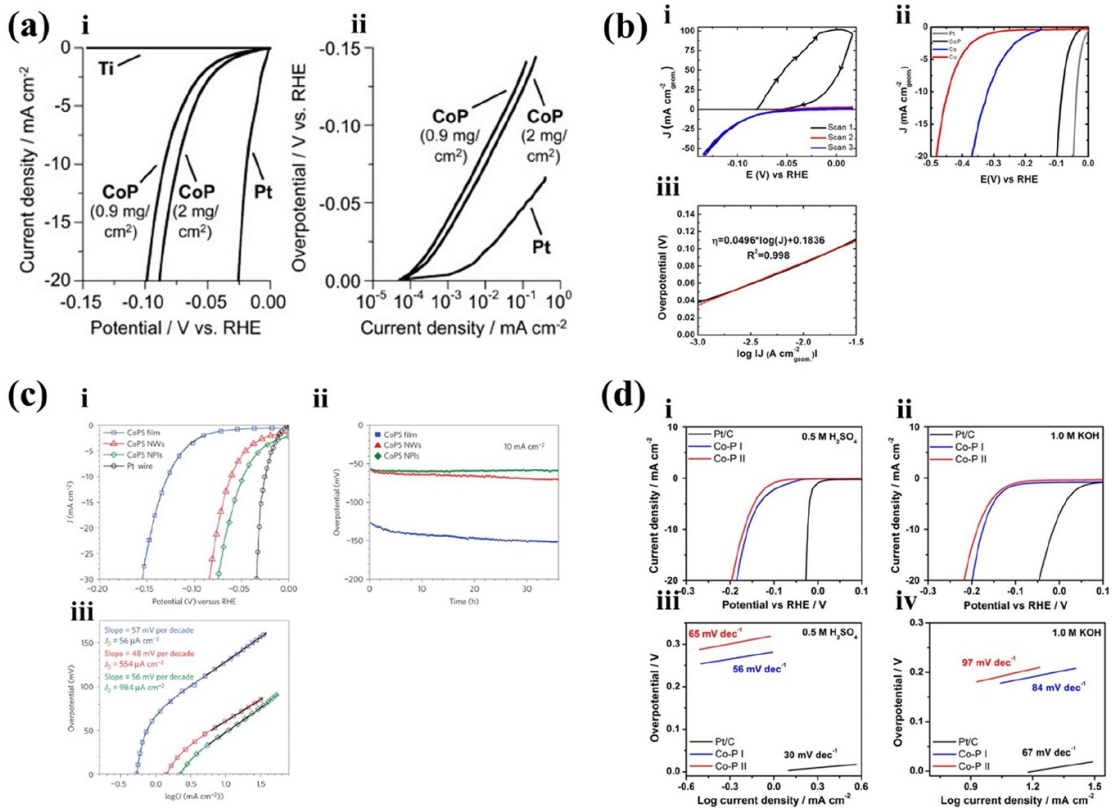

Figure 13. (**a**) (**i**) Polarization curve for CoP nanoparticle electrodes in acidic medium at loadings of 0.9 and 2 mg cm^{-2}. Data for Ti foil and Pt are included. (**ii**) Tafel plots for CoP and Pt electrodes. Reproduced with permission from [119] © 2014 WILEY-VCH Verlag GmbH & Co. KGaA, Weinheim, (**b**) (**i**) Voltammetric data for CoP thin films on glassy carbon in acidic medium. (**ii**) J–V data for Pt, CoP, Co, and Cu. (**iii**) Tafel plot of CoP from the data in panel (**ii**). Reproduced with permission from [120] Copyright (2014) American Chemical Society. (**c**) (**i**) J–V curves after iR correction for CoPS electrodes (film, blue; NWs, red; NPls, green) and a Pt wire (black). (**ii**) Long-term stability test for CoPS electrodes at a current density of 10 mA cm^{-2}. (**iii**) Tafel plot for the data presented in (**i**). Reproduced with permission from [117] © 2015, Springer Nature. (**d**) Voltammetric curves of CoP samples and Pt/C in (**i**) acidic (0.5 M H_2SO_4) and (**ii**) alkaline (1.0M KOH) conditions. The corresponding Tafel slopes are shown in (**iii**) and (**iv**). Reproduced with permission from ref. [121] Copyright (2018) American Chemical Society.

in current or loss in stability over time. By contrast, the $Ni_{12}P_5$ electrocatalyst, although giving a lower electrocatalytic activity, showed better stability over time. It would appear that the metal-rich $Ni_{12}P_5$ phase is less intrinsically active than Ni_2P but is more stable in terms of hydrogen production with a lower corrosion current.

4.3. Cobalt phosphides

Popczun *et al* first reported in 2014 that CoP is a highly active and acid-stable HER catalyst [119]. CoP is a known HDS catalyst and is structurally different and compositionally distinct from Ni_2P. CoP particles are single-crystalline with observed lattice spacings of 2.4 Å, consistent with closely spaced (102) and (111) planes of MnP-type CoP.

Multi-faceted, hollow CoP nanoparticles were synthesized via reaction of Co nanoparticles with thioctylphosphine. CoP/Ti electrodes were constructed by depositing CoP nanoparticles on a Ti support, followed by annealing. Figure 13(a) shows the polarization curve for CoP nanoparticle electrodes in acidic medium and the Tafel plots. The HER activity was consistent among ten different CoP/Ti samples. The electrodes exhibited a value for η_{20} of 85 mV and Tafel slopes of 50 mV dec^{-1}. The catalysts showed stability in 0.5M H_2SO_4 for 24 h with no change in activity over 400 CV sweeps. The value for η_{20} changed to ~90 mV after 400 cycles. This demonstrated high stability under strongly acidic conditions. The chemistry of CoP was described with a mechanism in which the bond strength of adsorbed hydrogen is strong enough to promote optimal hydrogen coverage but is not so strong to impede desorption of H_2.

Liu and coworkers pioneered a low-temperature toptotactic transformation preparation of metal phosphide nanostructures [127]. CoP nanocrystals were decorated on carbon nanotubes (CoP/CNT). This was prepared by a low-temperature phosphidation process of Co_3O_4/CNT precursor with NaH_2PO_2. The catalyst displayed high HER activity, with a reported η_{10} of 122 mV and a Tafel slope of 54 mV dec^{-1}.

Using a similar synthesis approach, the same group grew nanoporous CoP nanowire arrays on CC [128]. The resulting CoP/CC catalyst sustained hydrogen production for 80 000 s in acidic media and showed a Tafel slope of 51 mV dec^{-1} and η_{10} of 67 mV. This group has developed this novel approach to prepare binder-free 3D metal phosphide arrays [129] and nanowires [130] on Ti plates. The Ti-supported CoP nanosheet arrays exhibited a Tafel slope of 43 mV dec^{-1} and η_{10} of 90 mV while the CoP nanowires on Ti showed a Tafel slope of 65 mV dec^{-1} and η_{20} of 95 mV.

Saadi *et al* synthesized an amorphous CoP film on Cu through cathodic deposition from a solution of Co^{2+} in boric acid and H_2PO^{2-} [120]. Figure 13(b) shows the J–V curves for CoPS Tafel plots and stability over more than 30 h. After measuring HER, the Co:P ratio was 1:1, suggesting that the initial high-valent Co and P species present in the original catalyst are removed under HER conditions. This *in situ* film purification yields an active electrocatalyst, which displayed a Tafel slope of 50 mV dec^{-1} and η_{10} of 85 mV.

Caban-Acevedo *et al* predicted that HER catalytic activity of metal chalcogenides can be improved by tuning the hydrogen adsorption free energy through modifying the composition of CoS_2, figure 14(a), while preserving the pyrite structure [117]. The crystal structure of the resulting CoPS is similar to CoS_2 but shows dumbbells with a homogeneous distribution of P^{2-} and S^- anions. CoPS has one less valence electron than CoS_2 and is a semiconductor isoelectronic to iron pyrite. Since the Co octahedra in CoPS have P^{2-} ligands with higher electron-donating character than S^- ligands, this pyrite can show higher HER catalytic activity than CoS_2. DFT was used to compute ΔG_H on the (100) surface of CoPS and was compared to CoS_2. The ΔG_H at Co sites of CoPS is more favorable than on CoS_2. The calculations also show that after spontaneous hydrogen adsorption at open P sites, ΔG_H at the adjacent Co sites becomes spontaneous and almost thermoneutral, comparable to that of platinum. The change in ΔG_H is due to reduction of Co^{3+} sites to Co^{2+} on hydrogen adsorption at an adjacent open P site and this enables oxidation of Co^{2+} to Co^{3+} after subsequent hydrogen adsorption. This flexibility in the metal oxidation state was not observed for CoS_2.

CoPS film, CoPS nanowires (NW), and CoPS nanoplate (NPl) electrodes were studied for HER performance in 0.5 M H_2SO_4 in comparison to Pt wire. The CoPS film, NW and NPl electrodes exhibited values for η_{10} of 128, 61, and 48 mV and Tafel slopes of 48, 56, and 57 mV dec^{-1}, see figure 13(c). The catalysts also showed long-term operational stability beyond 36 h with little change in the film morphology.

CoPS was compared with CoP (which included a minor CoP_2 impurity) and showed that the catalytic HER performance of CoPS electrodes is attributable to the ternary pyrite-type compound instead of CoP impurities or anion-substituted doping on surface of CoPS.

Huang *et al* prepared Co_2P nanorods which exhibited values for η_{20} of 167 mV in acid solution and 171 mV in alkaline solution [131]. The Faradaic yield of H_2 production was close to 100% and the HER process followed the Volmer–Heyrovsky reaction, with a Tafel slope of 51.7 mV dec^{-1} in acidic conditions. Co_2P nanorods are stable in both acidic and alkaline solution during H_2 production. The importance of the crystal structure of Co_2P (orthorhombic) was highlighted. Co and P in Co_2P are similar to hydride and proton acceptors in Ni_2P. Similarities in the electronic nature of Co and P implied that the catalytic mechanism for HER would be the same in Co_2P and in Ni_2P.

Pan *et al* prepared a range of CoP-based electrocatalysts, including Co_2P, CoP, heterostructures interfaced with CNTs and with N-doped CNTs (NCNTs) *via* a thermal decomposition approach [132]. The catalytic activity followed the order CoP/NCNTs > Co_2P/NCNTs > CoP/CNTs > Co_2P/CNTs > CoP > Co_2P. The higher activity of CoP compared to Co_2P is related to the difference in coordination environments for Co and the higher phosphorous content in CoP. In addition, the strong interactions between CoP and carbon materials, and the doping of N atoms in the NCNTs further enhance the activity in the heterostructured materials. Furthermore, the high surface area in the CoP catalysts (44.2 $m^2\ g^{-1}$) compared to Co_2P (26.9 $m^2\ g^{-1}$) catalysts also promoted HER activity. Differences in the catalyst morphology were discussed. The rod-like morphology of CoP can enhance the efficiency of interfacial electron transfer, for example. The as-synthesized CoP/NCNTs catalysts exhibit the best electrocatalytic activity for HER in 0.5M H_2SO_4. A low onset overpotential of 32 mV, a small Tafel slope of 49 mV dec^{-1}, a high j_0 of 320 μA cm^{-2}, and η_{20} of 97 mV were reported. Stability was tested by CV scanning over 1000 cycles, at a scan rate of 50 mV s^{-1}, after which the LSV curve was unchanged from the first cycle.

Sumboja *et al* prepared CoPs for HER, in acidic and alkaline media [121]. Samples of CoP were synthesized using precursors containing acetate (labeled CoP I) or acetylacetonate (labeled CoP II). CoP I had a higher Co_xP content (92.5 wt%) compared to CoP II (63.5 wt%), to which was attributed the enhanced HER activity of CoP I in acid. However, both catalysts were active for HER in neutral and alkaline conditions. Figure 13(d) shows J–V of CoP samples and Pt/C in acidic (0.5 M H_2SO_4) and alkaline (1.0 M KOH) conditions, together with the corresponding Tafel slopes.

Cobalt oxides present in the Co-material were proposed to also be beneficial for the HER activity in alkaline conditions. The CoO_x is supposed to promote the dissociation of water due to the affinity of OH^- to Co^{2+} and Co^{3+}. Values for η_{10} of 160 and 169 mV were found in acidic electrolyte for the higher and lower

CoP content materials, respectively. These overpotentials are comparable to other forms of CoPs measured in acidic electrolytes—urchin-like CoP, 105 mV [133]; CoP nanowires, 110 mV [134]; CoP nanosheets, 164 mV [134]; CoP microparticles, 202 mV [135]; CoP nanoparticles, 221 mV [134]; and CoP microspheres, 226 mV [127].

In alkaline media the values for η_{10} were 175 and 188 mV fpr CoP I and CoP II, respectively, indicating that larger overpotentials are required to drive the HER in alkaline conditions. This compared to FeP_2 nanowires, 189 mV [136]; FeP nanowires, 194 mV [136]; and MoP nanoparticles, 276 mV [137]. Due to Tafel slopes in excess of 40 mV dec^{-1} for the CoP catalysts in both acidic and alkaline media, the authors concluded that HER is most likely to proceed via a Volmer–Heyrovsky mechanism.

In acid the CoP catalysts showed degradation of no more than 15.5% during 13 h of stability tests, which was better than the degradation of the Pt/C catalyst. In alkaline electrolyte, CoP shows only 4% degradation after 13 h of testing, compared to 19% for Pt/C catalyst.

Wu *et al* studied the pyrite structured ternary compound CoPS as an earth-abundant catalyst for photoelectrochemical hydrogen production in acidic environment [118]. Large single crystals of CoPS, with selectively exposed (100) and (111) facets, were synthesized and the corresponding HER activities were measured. Tafel slopes of 109 and 86 mV dec^{-1} were recorded for the (100) and (111) facets, respectively. The CoPS (100) surface contains intact PS^{3-} dimer dumbbells that are electron rich compared to S_2^{2-} in CoS_2, owing to the lower electronegativity of P compared to S. These electron-rich P sites provide strong H-binding sites. The adsorption of H onto a P site results in the reduction of Co^{3+} to Co^{2+}, which was proposed as a new site for subsequent facile H adsorption. The CoPS (111) with S- and P-terminations were considered. These (111) surfaces lack intact PS^{3-} dumbbells, but expose four symmetry-unique Co atoms, three of which are 4-coordinated and one of which is 3-coordinated. The electron rich 3-coordinated site preferentially adsorbs H atoms compared to the 4-coordinated Co sites, for both S- and P-terminated surfaces.

DFT computations of the free energies of H adsorption show that adsorption of the first H atom on the (111) facet is endergonic, while on the (100) facet this is exergonic, as shown in figure 14(b). The same is found for the second adsorbed H atoms so that the coverage of hydrogen appears to be an important factor in the activity of these catalysts.

In the low potential region (<0.35 V), the HER activity of (100) facet is superior to the (111) facet, which is reversed in the high potential region (>0.35 V). The differing HER activities are proposed to arise from differences in the energetics of H atom adsorption and the barriers to H–H recombination on these facets. At low potentials, the H adsorption process is rate limiting so the (100) facet is more active, while with increasing potential, H_2 recombination and desorption is the limiting step and the (111) facet shows lower desorption barriers.

4.4. Molybdenum phosphides

Molybdenum phosphide (MoP) is a well-known HDS catalyst [138]. DFT calculations showed that MoP can display properties similar to the platinum group metals, particularly the near zero free energy of hydrogen adsorption at certain H coverages [139]. The authors prepared bulk MoP and Mo_3P through tuning key synthesis parameters, including reaction temperature, and demonstrated the efficient HER activity of MoP, compared to Mo or Mo_3P. Tafel slopes of 54, 147, and 92 mV dec^{-1} were recorded in acidic medium for MoP, Mo_3O, and Mo, respectively. A Tafel slope of 48 mV dec^{-1} was measured for MoP in alkaline conditions. For MoP, the onset of hydrogen evolution was observed at ∼50 mV and the current density reached 30 mA cm^{-2} at a potential (η_{30}) of 180 mV. This demonstrates that phosphorization can modify the properties of Mo and tuning the degree of phosphorization has a strong impact on the HER activity and stability of the resulting catalysts. The catalytic activity of MoP persisted for 24 h, indicating good stability. The high HER activity was proposed to result from the presence of a closely interconnected network of MoP nanoparticles in the structure.

Kibsgaard *et al* incorporated sulfur into the surface of MoP, producing an MoPS (molybdenum phosphosulfide) catalyst [140]. The introduction of sulfur was achieved by post-sulfidation treatment of MoP in an atmosphere of H_2S. XRD showed that the crystal structure of MoP is not altered by introduction of sulfur. In acidic environment, this catalyst shows high activity and stability for HER, figure 15(a). A value for η_{10} of 86 mV for MoPS compared with 117 mV for MoP, for approximate loadings of ∼1 mg cm^{-2}. Increasing the loading of MoPS to ∼3 mg cm^{-2} reduces the η_{10} to 64 mV. Both MoP and MoPS exhibited similar Tafel slopes of ∼50 mV dec^{-1}. It was proposed that sulfur incorporation into MoP mitigates surface oxidation of the phosphide.

The stability of MoP and MoPS was assessed by 1000 continuous CV cycles, figure 15(B). The accelerated durability test was designed to represent the cycling expected for water (photo)electrolysis powered by

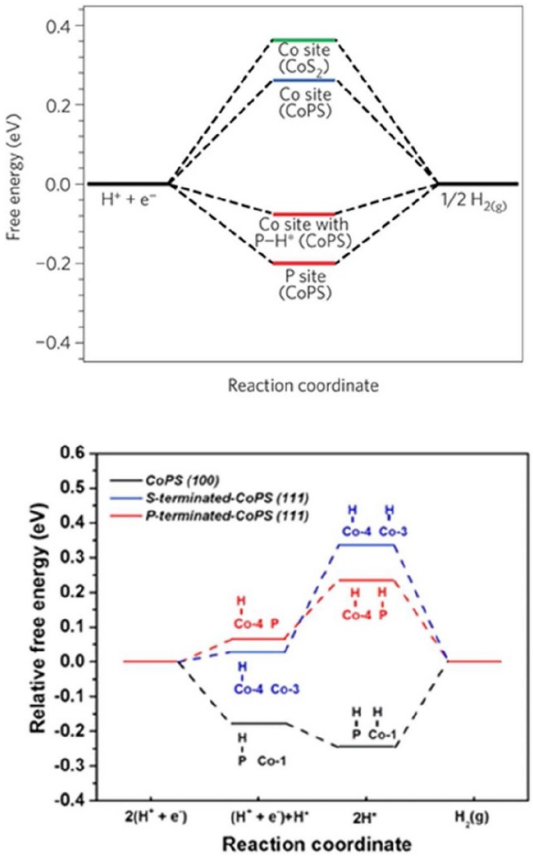

Figure 14. (**a**) Free energy diagram of H adsorption at various sites of CoS_2 and CoPS surfaces. Reproduced with permission from [117] © 2015, Springer Nature. (**b**) Computed free-energy changes (U = 0 V) of the lowest energy HER pathways on CoPS (100), S-terminated CoPS (111), and P-terminated CoPS (111) surfaces. At low potential, H adsorption process is rate limiting, but H_2 recombination/desorption becomes significant with increasing potential. Reproduced with permission from [118] Copyright (2018) American Chemical Society.

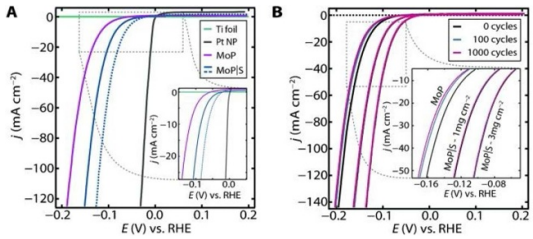

Figure 15. HER activity of MoP and MoPS. (**A**) Linear sweep voltammograms of MoP, MoPS, and Pt nanoparticles (NP). (**B**) Accelerated stability test. Initial and post-potential-cycling linear sweep voltammograms of MoP with an approximate loading of 1 mg cm^{-2} and of MoPS with approximate loadings of 1 and 3 mg cm^{-2}. MoPS remains perfectly stable whereas MoP experiences a slight decrease in current density upon increased potential cycling. Reproduced with permission from ref. [140] © 2014 WILEY-VCH Verlag GmbH & Co. KGaA, Weinheim.

intermittent renewable resources. MoP showed a slight decrease in activity with increased potential cycling. MoPS exhibited enhanced stability in this durability test, with overpotentials increasing by no more than 1 mV even at current densities larger than 100 mA cm^{-2}.

Sultana and Mullane reported on the HER activity of amorphous MoPS in both acidic and alkaline media [141]. The electrodeposited MoPS films contained oxygen and exhibited Tafel slopes of 36 mV dec^{-1} and 122 mV dec^{-1} in acidic and alkaline conditions, respectively. The authors reported that phosphorous was crucial to the alkaline HER activity and the samples remained stable after 20 h of electrolysis at 10 mA cm^{-2}. Huang *et al* deposited MoP nanoparticles on hierarchical carbonaceous scaffolds, MoP/NC [142]. This was followed by treatment with H_2S in Ar to create ultra-dispersed MoPS nanoparticles on the carbonaceous support, MoPS/NC. The authors measured values for η_{10} of 92 and 158 mV, for the S-containing catalyst, in acidic and alkaline media; this compared with values of 120 and 170 mV for the MoP/NC catalyst. Tafel

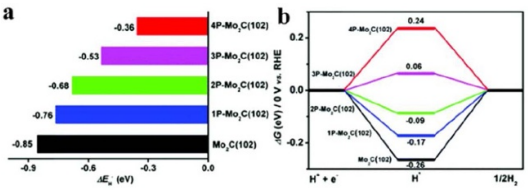

Figure 16. (**a**) Computed H binding energies ΔE_H and (**b**) the free energy changes ΔG_H for the HER over Mo_2C (102) and nP-doped Mo_2C (102) for n = 1–4. Reproduced with permission from [143], The Royal Society of Chemistry.

slopes of 52 and 50 mV dec^{-1} for MoP/NC and 56 and 57 mV dec^{-1} for MoPS/NC were recorded in acidic and alkaline conditions, respectively.

Controlled phosphorus doping was used to modify the electronic configuration of nanostructured Mo_2C [143]. Shi and coworkers controlled P-doping of Mo_2C by using MoO_x-phytic acid-polyaniline hybrids with tunable composition as precursors. The resulting catalysts consisted of hierarchical nanowires composed of P-doped Mo_2C nanoparticles integrated with conducting carbon and were denoted P-Mo_2C@C. The incorporation of P into Mo_2C increases the electron density around the Fermi level of Mo_2C. This weakens Mo–H bonding and improves the HER kinetics. With optimal doping, a ΔG_H approaching 0 eV presents a balance between the Volmer and Heyrovsky/Tafel steps in the HER kinetics. The optimal P content in P-Mo_2C@C nanowires was found to be 2.9 wt% and this catalyst delivered η_{10} of 89 mV and a Tafel slope of 42 mV dec^{-1} in acidic electrolytes. By contrast, pure Mo_2 C@C presented a Tafel slope of 64 mV dec^{-1}. The highest exchange current for 2.9% P-doped Mo_2 C@C was 180 μA cm^{-2}, which is very close to that of Pt/C (J_0 = 540 μA cm^{-2}). The Faradaic efficiency of 2.9% P-Mo_2 C@C is close to 100%.

When the Mo_2 C (102) surface is P-doped, the P atoms occupy the vacant interstitial sites or replace the C atoms of Mo_2C. With a larger atomic radius compared to carbon, the P atom prefers 4-fold hollow sites at the surface. It was proposed that the 1D nanostructure used in this work provides abundant space for H_2 bubble release and facilitates charge transfer in the axial dimension. Finally, as P doping was increased, an excess of phosphorous inhibits the HER activity, which highlights the importance of tunable control for optimal P-doping. Figure 16 shows the computed hydrogen binding energies (ΔE_H) and free energies changes per H (ΔG_H) for P-doped Mo_2C with varying P-content.

4.5. Ternary phosphide materials

Fang *et al* prepared CoP/MoP hybrid materials by doping Co into MoP to increase the intrinsic activity of MoP [144]. The measured Tafel slopes decreased from 84 to 60.5 mV dec^{-1} with increasing the Co/Mo ration from 0 to 0.5. These values suggest that HER occurs *via* a Volmer–Heyrovsky mechanism in which the slow adsorption of proton dominates the kinetics. Samples of $Co_{0.5}Mo_{0.5}P$ annealed at different temperatures were investigated for HER activity. For an annealing temperature of 650 °C, the authors reported the presence of hexagonal $CoMoP_2$, *h*-$CoMoP_2$. Increasing the annealing temperature to 1000 °C induced a change in phase from *h*-$CoMoP_2$ to CoMoP in which phosphorus is evaporated and the resulting CoMoP structure was less active than P-rich h-$CoMoP_2$.

Values for η_{10} of 250 and 283 mV were recorded for bulk MoP and CoP catalysts, respectively, compared with 50 mV for Pt foil. On adding Co to MoP, η_{10} decreases from 250 to 165 mV. The $Co_{0.5}Mo_{0.5}P$ catalyst showed an exchange current of 343 μA cm^{-2}, which is up to 6 and 16 times that of MoP and CoP catalysts. Figure 17(a) shows the Tafel plots for the CoMoP catalysts, together with the dependence of the Tafel slope on Co content (figure 17(b)). After 1000 CV cycles, figure 17(c), the $Co_{0.5}Mo_{0.5}P$ electrode showed a small increase of 11 mV in η_{10}, which indicated the stability of the catalyst under typical operating conditions.

Guan *et al* prepared high performance catalysts through the direct growth of catalyst materials in the form of well-aligned Mo-doped CoP nanoarrays on current collectors [145]. In this work, hollow Mo-doped CoP nanoarrays were prepared on CC starting from a MOF precursor. Mo-CoP arrays were transformed *in situ* into Mo-CoOOH with good OER properties, providing a means for overall water splitting. The spaces between the nanoarrays facilitate electrolyte penetration and the release of evolved gas bubbles. The electrical/mechanical connections between the active catalyst and the current collectors promote efficient electron transfer paths, which can also deliver long-term stability.

These materials were tested against control samples with similar structures: hollow CoP nanoarrays, hollow Co_3O_4 nanoarrays and noble metal based catalysts (Pt/C and Ir/C), all on CC. The Mo-CoP catalyst showed a small η_{10} of 40 mV, which was lower than those of CoP (160 mV) and Co_3O_4 (242 mV). The Tafel slope of Mo-CoP is 65 mV dec^{-1}, which is smaller than the corresponding Tafel slopes for CoP and Co_3O_4, which are 75 and 103 mV dec^{-1}, respectively. It appears that the overpotential can be reduced by

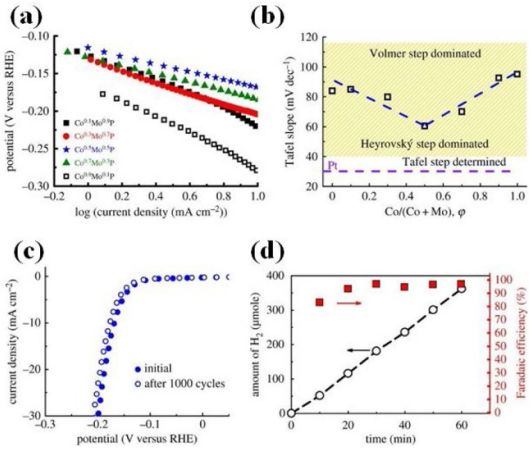

Figure 17. (**a**) Tafel plots of the $Co_zMo_{(1-z)}P$ catalysts. (**b**) The dependence of average Tafel slopes on the cobalt content. The Tafel slope of a Pt electrode is also included. (**c**) HER polarization curves of the $Co_{0.5}Mo_{0.5}P$ electrode before and after 1000 potential sweeps (**d**) Time dependence of the quantity of hydrogen produced experimentally (dashed line) and the Faradaic efficiency of the $Co_{0.5}Mo_{0.5}P$ catalyst at a fixed current density of 10 mA cm^{-2} for 60 min. Reproduced with permission from ref. [144].

phosphidation and formation of a ternary system through substitutional Mo-doping. At an overpotential of 100 mV, Mo-CoP exhibits a current density of 57 mA cm^{-2}, which is higher than the Pt/C catalyst, 47 mA cm^{-2}. Stability tests revealed that the Mo-CoP catalyst maintained 95% of the initial current density (~54 mA cm^{-2}) after 20 h of operation at 100 mV.

From DFT simulations, the origin of the superior Mo-CoP properties was proposed to be due to Mo doping giving lower free energy changes, ΔG_H, for hydrogen adsorption, compared to CoP. The hollow nanoarray structure has numerous nanograins, which is confirmed by atomic resolution STEM meaning that this structure has many active sites. Performance data for selected phosphide-based HER catalysts are presented in table 4, which can be found at the end of this review.

5. Accelerating materials discovery

In the preceding sections, we have also highlighted the complementary role of computational methods, and particularly DFT, in identifying active sites and the origin of the activity of catalyst materials for HER. This is driven by the observation that the Gibbs free energies of H adsorption at active sites of Pt and hydrogen producing enzymes were close to thermodynamically neutral, i.e. $\Delta G_H \approx 0$ eV, in accordance with the Sabatier principle [44, 146]. Thus, ΔG_H is considered an appropriate descriptor to assess the potential for a given material to catalyze the HER. This has paved the way for fast screening of candidate materials by computing ΔG_H for various sites and hydrogen coverages at the surface of modes of the catalyst and has informed design and fabrication methods to maximize exposure of active sites. Establishing simple relationships between chemical concepts and HER activity is also of interest.

However, as mentioned in the introduction, care must be taken with the application and interpretation of computational models. Describing the complexity of the catalyst surface and its environment represents a considerable challenge for first principles simulations. The relevance of computational results depends on the accuracy with which the models approximate the real system. While free energy calculations are the workhorse of computational materials discovery, with demonstrable efficacy, there are efforts to bridge the gap between simple surface, vapor-phase models and the finite-temperature catalyst-solvent interface [147, 148].

There are various strategies to account for the solvent and its role in the chemistry at the catalyst surface. The solvent can be incorporated implicitly, where the solvent is treated in an average way and described as a continuous medium, or explicitly, where the molecules that constitute the solvent are included in the computation [149].

Explicit solvation models can range in complexity from single to multiple layers of molecules at the catalyst surface [150–152]. Ping and coworkers examined the impact of water on the band positions of some common photocatalyst materials [150]. They compared results among approaches, including an explicit, single water layer, continuum solvation models (CSMs), and combinations of the two. The authors reported that, while CSMs were sufficient to account for the solvation shift in the band energies of hydrophobic surfaces, the inclusion of an explicit water layer was necessary to describe the stronger interactions at hydrophilic surfaces.

Skúlason and colleagues implemented a water bilayer in their model of the HER at Pt (111) [151]. By varying the number of H atoms in the bilayer, the authors could examine the effect of the electrode potential on the activation energies in the HER. This is because the H atoms were solvated in the bilayer—the protons remained in the bilayer while the electrons moved to the catalyst surface. In this way, their model described the Helmholtz double layer.

The treatment of such a system with DFT can be used to determine the effect of the solvent on the binding energies of reaction intermediates. However, DFT is a 0 K theory, and so cannot describe the temperature-dependent effects of a liquid solvent. Thus, an approach to modeling the solvent at finite temperatures is to implement molecular dynamics (MD). Classical MD simulations can be used to obtain an array of local minima in the solvent configuration, which are subsequently treated with DFT [149]. In classical MD, quantum effects and electronic degrees of freedom are neglected and molecule positions are determined by solving Newton's equations of motion. This necessitates the implementation of force fields, which must be parametrized for the system under study [153, 154].

Another approach to modeling finite temperature solvents, explicitly, is *ab initio* MD (AIMD). AIMD differs from classical MD in that it is based on quantum, rather than classical, mechanics [155]. Kronberg and colleagues compared AIMD with NEB in their study of the Volmer–Heyrovsky mechanism for the HER at an N-doped carbon nanotube [156]. The authors reported substantial discrepancies between the activation and reaction energies computed with the two methods and highlighted the importance of explicitly including interfacial dynamics when studying the HER at the catalyst-electrolyte interface. Cheng and coworkers used AIMD to examine the role of charge trapping during deprotonation of a surface-bound hydroxyl at rutile TiO_2 (110) [157]. Gono *et al* found that the explicit inclusion of water molecules in their models affected the overpotential for water oxidation at rutile TiO_2 by up to 0.5 V [152].

Van den Bossche and coworkers approximated the solvent by a polarizable dielectric continuum in their study of the HER at Pt surfaces [158]. The authors maintained a constant electrode potential by varying the concentration of counterions in the electrolyte, in response to changes in the number of electrons during the reaction. The results of this implicit approach compared favorably with the more rigorous and computationally expensive, 'extrapolation' approach [159, 160].

Chang *et al* used both implicit and explicit solvent models to examine the HER at sub-nm Au-Ag clusters [161]. In their implicit model, the authors computed the solvation energy of the nanoclusters and thereby adjusted the electron affinity to account for the water environment. The explicit model implemented AIMD to test the catalyst stability and introduce thermal effects.

Despite these advances in computational techniques to model the catalyst-electrolyte interface, descriptor-based approaches remain at the forefront of computation-driven design of new photocatalyst materials. Expanding on this theme and going beyond the usual application of DFT calculations to the HER, machine learning approaches are being investigated. In machine learning, the algorithm is trained on a known data set related to the catalytic descriptor of interest and the resulting machine learning function is then used to explore a wide range of potential materials at much lower cost than a full DFT-level simulation. In one example of this, Jäger and colleagues adopted a machine learning approach [146] in which they constructed a large data set of hydrogen adsorption energies on various sites of nanoclusters of MoS_2 and $Au_{40}Cu_{40}$, figure 18(a). This dataset was characterized by structural descriptors and used to train a model to predict the adsorption energy for an arbitrary site based on its description. The goal of this study was to establish how many data points were required to interpolate the potential energy surface and predict the hydrogen adsorption energy, ΔE_H, to an accuracy of 0.1 eV. Datasets consisted of 10 000 single-point DFT calculations of ΔE_H and comparisons were made between a number of structural descriptors: atom-centered symmetry functions [162]; many-body tensor representation [163]; and smooth overlap of atomic positions [164, 165]. The authors concluded that each of the aforementioned descriptors performed satisfactorily well, provided they were given a training set of sufficient size, which is a key consideration in developing machine learning models.

Another computational descriptor that can be used to assess the active sites of a catalyst surface is the Fermi softness, S_F [166]. This descriptor finds its analogue in frontier molecular orbital theory[167], which describes the spatial distribution of active sites of a molecule. The local Fermi softness at position r is defined as:

$$S_F(r) = -\int g(E,r) f'_T(E - E_F)\, dE$$

where $g(E,r)$ is the DOS projected at position r and $f'_T(E - E_F)$ is the derivative of the Fermi–Dirac distribution function at finite temperature. The negative of $f'_T(E - E_F)$ provides a weighting factor which reaches a maximum at E_F and this is included to reflect the greater contribution to bonding of states near the Fermi level. Huang *et al* benchmarked this descriptor in a study of transition metal surfaces before examining active sites of a one-dimensional MoS_2 edge [166]. Based on analysis of $S_F(r)$, figure 18(b), and subsequently

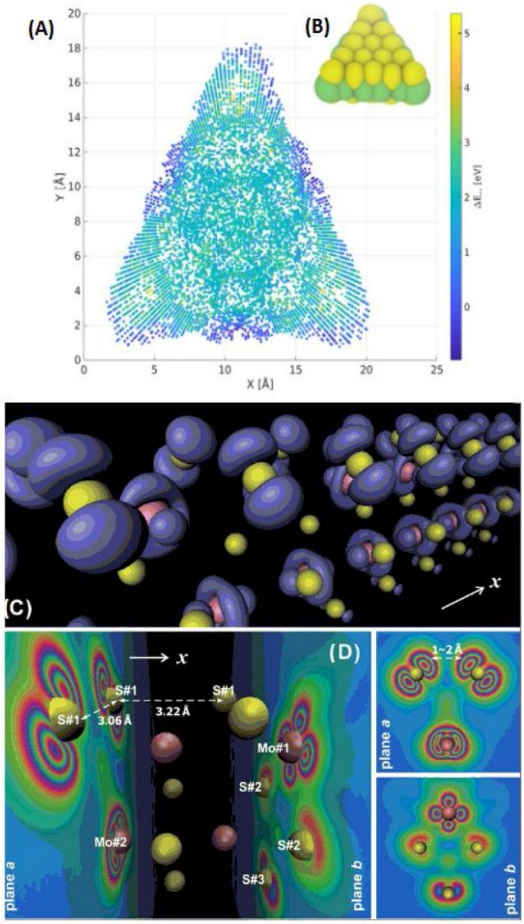

Figure 18. (**a**) Hydrogen position scan on the surface of a triangular-shaped MoS_2 cluster. The inset (**b**) shows the geometry of the MoS_2 cluster. Reproduced with permission from [146] (**c**) A 3D view of the calculated $S_F(r)$ isosurface (blue, on which $S_F = 55$ /keV Å^{-3}) at the MoS_2 edge. (**d**) The $S_F(r)$ is projected onto two planes, which are normal to the x-direction. Reproduced with permission from [166]. © 2016 WILEY-VCH Verlag GmbH & Co. KGaA, Weinheim.

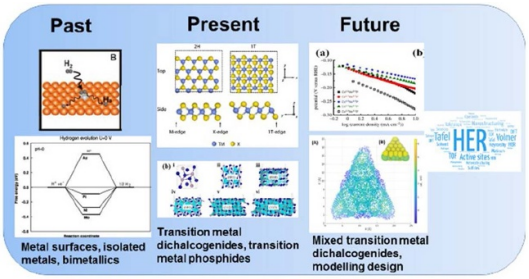

Figure 19. Highlighting the evolution of HER materials from metals, through low dimensional materials and phosphides to mixed cation catalysts and the role of modeling. The word cloud shows keywords used in this field. Adapted with permission from [15, 48, 116, 144, 166, 170].

confirmed by NEB calculations, the authors identified a subtlety in the reactivity at the MoS_2 edge: an anisotropy exists which promotes the HER at intra-S-dimer bridge sites, relative to inter-S-dimer bridge sites.

Ran and colleagues established a relationship between the HER activity and bond electronegativity in a study of TMDs [168]. Citing a trial-and-error approach in existing endeavors to activating and optimizing catalysts for HER, the authors implemented a high-throughput first-principles strategy to identify a universal design principle. The study began with 2H-MoS_2 doped with other TMs and examined H adsorption at S-sites neighboring the TM-dopant. The authors presented a formula that describes the characteristic S-H bonding electron number, based on the local properties of the active site. The descriptor, Ψ, takes into account bond electronegativity, coordination numbers, and valence electrons, and was used to predict potential HER catalysts with high activities; although experimental confirmation is required to confirm the validity of such predictions.

Table 2. Sulfur-based HER catalysts.

Materials	Overpotential (mV)	Current Density (mA cm^{-2})	Exchange Current Density (μA cm^{-2})	H_2 Evolution Rate (μmol g^{-} h^{-})	Tafel Slope (mV dec^{-})	Ref.
MoS_2 NPs			0.13–0.45		55–60	[51]
MoS_2 (strain + vacancies)	170	10			60	[82]
MoS_2/Au			5–25		73–85	[65]
MoS_2/MoS_2					81	[87]
MoS_2/WS_2					73	[87]
MoS_2/CC	171	10			50	[99]
	215	100				
MoS_2/CoS_2/CC	118	10			37	[99]
	159	100				
MoS_2/GCE	104	10	91		53	[85]
$CoMoS_x$	∼200	5				[100]
2H-WS_2					110	[79]
1T-WS_2			20		60	[79]
TaS_2/Au	65–100	10	100–179		33–42	[66]
CoS_2/CFP	90	10			67	[75]
N and S co-doped porous carbon—derived from human hair	97	10		480 mmol/g/h High specific surface area (up to 830.0 m^2 g^{-1})	57	[171]
S,N-codoped MoP	57, 104 (acid)	1, 10	56 (acid)		45 (acid)	[172]
	20, 94 (base)	1, 10	480 (base)		59 (base)	
MoP on S,N-codoped graphene	49, 99 (acid)	1, 10	150 (acid)		54 (acid)	[172]
	11, 49 (base)	1, 10	460 (base)		31 (base)	
MoPS	117	10	200		50	[140]
	180	100	(1 mg cm^{-2})			
			570			
			(3 mg cm^{-2})			
S-doped g-C_3N_4				12.16 μmol h^{-1}		[173]
ZnS/g-C_3N_4 heterojunction				713.68	66	[174]

Table 3. Selenium-based HER catalysts.

Materials	Overpotential (mV)	Current densities (mA cm^{-2})	Exchange current density (μA cm^{-2})	H_2 Evolution Rate (μmol g^{-1} h^{-1})	Tafel slope (mV dec^{-1})	Ref.
$MoSe_2$	41	2	100		77	[175]
	200	35				
$NiSe_2$	117	10	4.7		32	[176]
$Ni_{0.33}Co_{0.67}Se_2$	65	10	184		35	[110]
$CoSe_2$/CP	137	10	4.9		40	[81]
	150	20				
	181	100				
Polymorphic $CoSe_2$	150	10			31	[101]
$MoSe_2$ nanosheets	290	10			101	[177]
$MoSe_2$/RGO	115	10			69	[177]
Amorphous $MoSe_x$	270	10			60	[97]
Amophous $CoSe_x$	135	10	64		62	[98]
$NiSe_2$ nanosheets	198	10			72.1	[178]
NiSe nanoflakes	217	10			28.6	[178]
EG/$Co_{0.85}Se$/NiFe	260	10	220		160	[179]
Pt/np-$Co_{0.85}Se$	55	10			35	[180]

Hu *et al* explored the mechanism for HER on pristine CoP using first principles simulations [169]. The most stable surface facet on CoP is (011), followed by (110), (111), and (100). The (011) facet exhibits the highest surface packing density. From the DFT results, the Co bridge sites and P top sites are able to adsorb hydrogen atoms with a free energy change that is close to 0 eV. Importantly, and going beyond many studies

Table 4. Phosphorus-based HER catalysts.

Materials	Overpotential (mV)	Current densities (mA cm^{-2})	Exchange current density (μA cm^{-2})	H_2 Evolution rate (μmol/g/h)	Tafel slope (mV dec^{-1})	Ref.
P-TCN				670		[181]
GCN				90		[181]
Ni_2P as recv.					128	[126]
Ni_2P (6 h ball-milling)					79	[126]
Ni_2P (9 h ball-milling)					84	[126]
$Ni_{12}P_5$					108	[126]
P-Mo_2C@C-NW	89	10	180		42	[143]
Micro-fibrous P				633		[122]
Smashed-fibrous P				684		[122]
CoPS film	128	10	56		48	[117]
CoPS NW	61	10	554		56	[117]
CoPS NPl	48	10	984		57	[117]
BP/CN				427 (>420 nm) 101 (>780 nm)		[123]
Co-P/BP				375		[124]
Co_2P nanorods	167 (acid) 171 (base)	20 20			52 (acid)	[131]
CoP/Ti	90	20	140		50	[119]
CoP/NCNT	99	20	320		49	[132]
$Co_{0.5}Mo_{0.5}P$	165	10	343		61	[144]
CoP I	160 (acid) 175 (base)	10			56 (acid) 84 (base)	[121]
CoPS (100)			39		109	[118]
CoPS (111)			5		86	[118]
Mo-CoP nanoarrays	40	10			65	[145]

where single H atom adsorption is studied and temperature/pressure are neglected, both the role of hydrogen coverage and *ab initio* thermodynamics were considered to make better contact with experimental set-ups.

In exploring coverage effects on the CoP (111) surface, which is claimed to be present in typical nanostructures of CoP, the authors showed that at a hydrogen coverage of 25% H atoms is strongly adsorbed at cobalt bridge sites, with computed ΔG_H of *ca.* −0.6 eV. Upon increasing the hydrogen coverage beyond 25%, adsorption at cobalt bridge and phosphorus sites is possible and there are some dependencies of ΔG_H on which sites are occupied. The value of ΔG_H is close to zero for these coverages so that cobalt bridge sites and phosphorus top sites are active for HER on the (111) surface. For coverages up to 100% hydrogen, more than one H atom can adsorb on Co atoms.

From *ab intio* thermodynamics, extremely low hydrogen pressures result in the clean surface being the most stable. At typical ambient pressures, 75% hydrogen coverage is most stable. The authors conclude that the (111) surface of CoP is the most active facet for high and stable HER activity.

Liang *et al* presented DFT studies to show that the different surface facets in a catalyst can show very different HER properties [116]. They show that the surface stability of Co_2P facets goes in the order: (112) > (010) > (113) >(101) > (001). To examine the HER activity, the usual Gibbs free energy of hydrogen adsorption, ΔG_H was used to evaluate HER activity. The optimum ΔG_H value for the five facets is in the following order: (113) L1 ≈ (001) L1 < (112) L1 < (101) L5 < (010) L5 < (010) L4, where L1, L3, L4, and L5 indicate specific adsorption sites. Given that the surface energy of the (113) facet is smaller than that of the (001) facet, Co_2P catalysts that expose the (113) surface would be proposed as active catalysts for HER. The effect of the Co–H distance on the charge transfer from Co to adsorbed H can be examined. A shorter Co–H bond length induces larger charge transfer from Co to H. The 'Co_s' species has a stronger effect on ΔG_H than other Co species. Considering the Fermi levels, these are found in a valley of the DOS for the (001) and (101) facets and on a hill for (112), which is in agreement with the proposed HER activity. Finally, a linear relationship between the Co–H bond lengths and the computed ΔG_H was established.

6. Conclusions

The importance of the HER in both electrochemistry and renewable fuel is undeniable. It serves as both the key half reaction for production of high purity hydrogen from water splitting but also as a side reaction in other technologies. Noble metals have been widely studied for the HER and still act as a benchmark for any

potential catalyst materials. However, recent years have seen an upsurge of interest in using chalcogens and phosphides for the HER reaction and there is a bewildering number of papers on this topic. In figure 19, we summarise what we see as the evolution from metals through the current high performance, low dimensional materials and phosphides. The future includes heterostructures, mixed cation catalysts and the important role of modeling in catalyst design.

However, despite all this work, there is still no ideal, scalable HER technology. One issue that should be addressed is the characterization and reporting of the HER catalysts and their activity, similar to the protocols for reporting solar cells, where standards have been adopted.

In this regard tables 1, 2, 3 and 4 present a compilation of data from HER studies referenced in this review and some additional references where metal sulfides, selenides, and phosphides were explored. If we consider the five characteristics presented in these tables, we can immediately see that not every study of HER presents and discussed these data. Tafel slopes tend to be most widely reported, along with overpotentials. These would be sensitive to details around composition, preparation, cycling, test conditions, *etc*, and it would be of significant benefit to report other characteristics such as exchange current density, H_2 evolution rate, H_2 evolution after a defined number of cycles or over a predetermined time; these latter two will be crucial for the large-scale performance of the HER catalyst. Reproducible preparation methodologies will also be needed so that results can be reproduced and the feasibility of scale-up of production can be assessed. In addition, there will also be a requirement to assess the cost/economic aspects and investigate the life cycle analysis of these catalysts. As one example, although cobalt is a promising metal cation for HER catalysts, e.g. $CoSe_2$ or CoP, it is a critical raw material with a huge demand from the battery sector and issues around its mining and extraction.

Despite the discussion above, the results of the papers discussed in this review show that chalcogenides and phosphides are extremely promising HER materials. Exploiting the advances in controlled synthesis, heterostructuring and characterization has allowed fine control of structure and composition, e.g. the amount of phosphorous or the relative amounts of two cations, which can be used to enhance the HER in these materials.

Key fundamental properties of these materials include the high lying electronic states with metallic character, which means that the free energy of hydrogen adsorption can be close to 0 eV and thus drive HER. In addition, the introduction of a second metal in a ternary structure, e.g. Mo/Co-containing catalysts can modulate the electronic structure and further promote the HER activity. Low dimensional structures show high surface to volume ratios, which can have a high density of active sites; however, of course, the 2D dichalcogenides have an inactive basal plane, so strategies to activate the exposed areas or facets are also valuable. Heterostructures can tune light absorption for photochemical HER, as well as tuning the density of active sites and charge localization. Finally, we have to ensure that the catalyst is stable under the desired use conditions, e.g. acid environment, applied voltage, expected number of cycles or time under which it is used.

As we drive toward the dream of clean, efficient hydrogen production, advances in multiple areas will only help to bring us closer to a usable HER catalyst. In synthesis, using atomic layer deposition to deposit well controlled amounts of finely dispersed active materials will be an extremely valuable advance, producing highly active materials, but using small amounts of valuable metals. In characterization, advances in microscopy and *operando* methods will allow a deeper understanding of HER catalysts and give key insights into the features that drive a good catalyst. Finally, the power of computational modeling will drive rapid screening of a multitude of candidate materials, allowing only the most suitable to be prepared and tested, giving significant savings in time and cost while growing our understanding of the fundamentals of HER catalysts.

Acknowledgments

We acknowledge support from Science Foundation Ireland through the Horizon 2020 M-ERA.net cofund program, project RATOCAT, Grant No. 685451 and SFI 17/M-ERA/3418.

ORCID iDs

Stephen Rhatigan https://orcid.org/0000-0002-9652-468X
Michael Nolan https://orcid.org/0000-0002-5224-8580

References

[1] Callejas J F, Read C G, Roske C W, Lewis N S, Schaak R E and Synthesis C 2016 Properties of metal phosphide catalysts for the hydrogen-evolution reaction *Chem. Mater.* **28** 6017–44

[2] Wallace J S and Ward C A 1983 Hydrogen as a fuel *Int. J. Hydrogen Energy* **8** 255–68
[3] Pinaud B A *et al* 2013 Technical and economic feasibility of centralized facilities for solar hydrogen production via photocatalysis and photoelectrochemistry *Energy Environ. Sci.* **6** 1983–2002
[4] US Department of Energy 2012 Multi-year research, development, and demonstration plan *Fuel Cell Technologies Office* https://www.energy.gov/sites/prod/files/2014/12/f19/fcto_myrdd_full_document.pdf
[5] European Comission 2011 Materials roadmap enabling low carbon energy technologies *European Staff Working Paper* https://setis.ec.europa.eu/system/files/Materials_Roadmap_EN.pdf
[6] Yan Y, Xia B Y, Zhao B and Wang X 2016 A review on noble-metal-free bifunctional heterogeneous catalysts for overall electrochemical water splitting *J. Mater. Chem.* A **4** 17587–603
[7] Zou X and Zhang Y 2015 Noble metal-free hydrogen evolution catalysts for water splitting *Chem. Soc. Rev.* **44** 5148–80
[8] Hu C, Zhang L and Gong J 2019 Recent progress made in the mechanism comprehension and design of electrocatalysts for alkaline water splitting *Energy Environ. Sci.* **12** 2620–45
[9] Vesborg P C K, Seger B and Chorkendorff I 2015 Recent development in hydrogen evolution reaction catalysts and their practical implementation *J. Phys. Chem. Lett.* **6** 951–7
[10] Browne M P, Stafford S, O'Brien M, Nolan H, Berner N C, Duesberg G S, Colavita P E and Lyons M E G 2016 The goldilocks electrolyte: examining the performance of iron/nickel oxide thin films as catalysts for electrochemical water splitting in various aqueous NaOH solutions *J. Mater. Chem.* A **4** 11397–407
[11] Mohammed-Ibrahim J and Sun X 2019 Recent progress on earth abundant electrocatalysts for hydrogen evolution reaction (HER) in alkaline medium to achieve efficient water splitting – A review *J. Energy Chem.* **34** 111–60
[12] Wei J, Zhou M, Long A, Xue Y, Liao H, Wei C and Xu Z J 2018 Heterostructured electrocatalysts for hydrogen evolution reaction under alkaline conditions *Nano-Micro Lett.* **10** 75
[13] Xiao P, Chen W and Wang X 2015 A review of phosphide-based materials for electrocatalytic hydrogen evolution *Adv. Energy Mater.* **5** 1500985
[14] Dubouis N and Grimaud A 2019 The hydrogen evolution reaction: from material to interfacial descriptors *Chem. Sci.* **10** 9165–81
[15] Nørskov J K, Bligaard T, Logadottir A, Kitchin J R, Chen J G, Pandelov S and Stimming U 2005 Trends in the exchange current for hydrogen evolution *J. Electrochem. Soc.* **152** J23-J26
[16] Benck J D, Hellstern T R, Kibsgaard J, Chakthranont P and Jaramillo T F 2014 Catalyzing the hydrogen evolution reaction (HER) with molybdenum sulfide nanomaterials *ACS Catal.* **4** 3957–71
[17] Luo F, Choi C H, Primbs M J M, Ju W, Li S, Leonard N D, Thomas A, Jaouen F and Strasser P 2019 Accurate evaluation of active-site density (SD) and turnover frequency (TOF) of PGM-free metal–nitrogen-doped carbon (MNC) electrocatalysts using CO cryo adsorption *ACS Catal.* **9** 4841–52
[18] Trasatti S and Petrii O A 1991 Real surface area measurements in electrochemistry *Pure & Appl. Chem.* **63** 711
[19] Shinagawa T, Garcia-Esparza A T and Takanabe K 2015 Insight on Tafel slopes from a microkinetic analysis of aqueous electrocatalysis for energy conversion *Sci. Rep.* **5** 13801
[20] Gorlin Y and Jaramillo T F 2010 A bifunctional nonprecious metal catalyst for oxygen reduction and water oxidation *J. Am. Chem. Soc.* **132** 13612–4
[21] Anantharaj S, Ede S R, Karthick K, Sam Sankar S, Sangeetha K, Karthik P E and Kundu S 2018 Precision and correctness in the evaluation of electrocatalytic water splitting: revisiting activity parameters with a critical assessment *Energy Environ. Sci.* **11** 744–71
[22] Chen Z, Duan X, Wei W, Wang S and Ni B-J 2019 Recent advances in transition metal-based electrocatalysts for alkaline hydrogen evolution *J. Mater. Chem.* A **7** 14971–5005
[23] Gao Y, Li H, Wang J, Ma J and Ren H 2019 New insight on hydrogen evolution reaction activity of MoP2 from theoretical perspective. *Nanomaterials* **9** 1270
[24] Yang L, Liu P, Li J and Xiang B 2017 Two-dimensional material molybdenum disulfides as electrocatalysts for hydrogen evolution. *Catalysts* **7** 285
[25] Föttinger K and Rupprechter G 2014 In situ spectroscopy of complex surface reactions on supported Pd–Zn, Pd–Ga, and Pd(Pt)–Cu nanoparticles *Acc. Chem. Res.* **47** 3071–9
[26] Zhu Y, Wang J, Chu H, Chu Y-C and Chen H M 2020 In situ/operando studies for designing next-generation electrocatalysts *ACS Energy Lett.* **5** 1281–91
[27] Li Y H, Li C and Yang H G 2017 Quantitative analysis of the PtO structure during photocatalytic water splitting by operando XAFS *J. Mater. Chem.* A **5** 20631–4
[28] Zhu Y, Chen H-C, Hsu C-S, Lin T-S, Chang C-J, Chang S-C, Tsai L-D and Chen H M 2019 Operando unraveling of the structural and chemical stability of P-substituted CoSe2 electrocatalysts toward hydrogen and oxygen evolution reactions in alkaline electrolyte *ACS Energy Lett.* **4** 987–94
[29] Wygant B R, Kawashima K and Mullins C B 2018 Catalyst or precatalyst? the effect of oxidation on transition metal carbide, pnictide, and chalcogenide oxygen evolution catalysts *ACS Energy Lett.* **3** 2956–66
[30] Deng Y, Ting L R L, Neo P H L, Zhang Y-J, Peterson A A and Yeo B S 2016 Operando raman spectroscopy of amorphous molybdenum sulfide (MoSx) during the electrochemical hydrogen evolution reaction: identification of sulfur atoms as catalytically active sites for H+ reduction *ACS Catal.* **6** 7790–8
[31] Daviddi E, Gonos K L, Colburn A W, Bentley C L and Unwin P R 2019 Scanning electrochemical cell microscopy (SECCM) chronopotentiometry: development and applications in electroanalysis and electrocatalysis *Anal. Chem.* **91** 9229–37
[32] Bentley C L, Kang M, Maddar F M, Li F, Walker M, Zhang J and Unwin P R 2017 Electrochemical maps and movies of the hydrogen evolution reaction on natural crystals of molybdenite (MoS2): basal vs. edge plane activity *Chem. Sci.* **8** 6583–93
[33] Bentley C L, Kang M and Unwin P R 2017 Nanoscale structure dynamics within electrocatalytic materials *J. Am. Chem. Soc.* **139** 16813–21
[34] Zhang Y, Gao L, Hensen E J M and Hofmann J P 2018 Evaluating the stability of Co2P electrocatalysts in the hydrogen evolution reaction for both acidic and alkaline electrolytes *ACS Energy Lett.* **3** 1360–5
[35] Lassalle-Kaiser B, Zitolo A, Fonda E, Robert M and Anxolabéhère-Mallart E 2017 In situ observation of the formation and structure of hydrogen-evolving amorphous cobalt electrocatalysts *ACS Energy Lett.* **2** 2545–51
[36] Saadi F H, Carim A I, Drisdell W S, Gul S, Baricuatro J H, Yano J, Soriaga M P and Lewis N S 2017 Operando spectroscopic analysis of CoP films electrocatalyzing the hydrogen-evolution reaction *J. Am. Chem. Soc.* **139** 12927–30
[37] Wang X L, Liu W, Yu -Y-Y, Song Y, Fang W Q, Wei D, Gong X-Q, Yao Y-F and Yang H G 2016 Operando NMR spectroscopic analysis of proton transfer in heterogeneous photocatalytic reactions *Nat. Commun.* **7** 11918

[38] Tanimu A and Alhooshani K 2019 Advanced hydrodesulfurization catalysts: a review of design and synthesis *Energy Fuels* **33** 2810–38
[39] Vasudevan P T and Fierro J L G 1996 A review of deep hydrodesulfurization catalysis *Catal. Rev.* **38** 161–88
[40] Yan Y, Xia B, Xu Z and Wang X 2014 Recent development of molybdenum sulfides as advanced electrocatalysts for hydrogen evolution reaction *ACS Catal.* **4** 1693–705
[41] Raybaud P, Hafner J, Kresse G, Kasztelan S and Toulhoat H 2000 Ab initio study of the H2–H2S/MoS2 Gas–solid interface: the nature of the catalytically active sites *J. Catal.* **189** 129–46
[42] Nidola A and Schira R 1986 New sulphide coatings for hydrogen evolution in KOH electrolysis *Int. J. Hydrogen Energy* **11** 449–54
[43] Sobczynski A 1991 Molybdenum disulfide as a hydrogen evolution catalyst for water photodecomposition on semiconductors *J. Catal.* **131** 156–66
[44] Hinnemann B, Moses P G, Bonde J, Jørgensen K P, Nielsen J H, Horch S, Chorkendorff I and Nørskov J K 2005 Biomimetic hydrogen evolution: MoS2 nanoparticles as catalyst for hydrogen evolution *J. Am. Chem. Soc.* **127** 5308–9
[45] Sobczynski A, Yildiz A, Bard A J, Campion A, Fox M A, Mallouk T, Webber S E and White J M 1988 Tungsten disulfide: a novel hydrogen evolution catalyst for water decomposition *J. Phys. Chem.* **92** 2311–5
[46] Bonde J, Moses P G, Jaramillo T F, Nørskov J K and Chorkendorff I 2009 Hydrogen evolution on nano-particulate transition metal sulfides *Faraday Discuss.* **140** 219–31
[47] Tsai C, Chan K, Abild-Pedersen F and Nørskov J K 2014 Active edge sites in $MoSe_2$ and WSe_2 catalysts for the hydrogen evolution reaction: a density functional study *Phys. Chem. Chem. Phys.* **16** 13156–64
[48] Tsai C, Chan K, Nørskov J K and Abild-Pedersen F 2015 Theoretical insights into the hydrogen evolution activity of layered transition metal dichalcogenides *Surf. Sci.* **640** 133–40
[49] Bollinger M V, Jacobsen K W and Nørskov J K 2003 Atomic and electronic structure of MoS_2 nanoparticles *Phys. Rev.* B **67** 085410
[50] Lauritsen J V, Bollinger M V, Lægsgaard E, Jacobsen K W, Nørskov J K, Clausen B S, Topsøe H and Besenbacher F 2004 Atomic-scale insight into structure and morphology changes of MoS_2 nanoclusters in hydrotreating catalysts *J. Catal.* **221** 510–22
[51] Jaramillo T F, Jørgensen K P, Bonde J, Nielsen J H, Horch S and Chorkendorff I 2007 Identification of active edge sites for electrochemical H_2 evolution from MoS_2 nanocatalysts *Science* **317** 100–2
[52] Chandrasekaran S, Yao L, Deng L, Bowen C, Zhang Y, Chen S, Lin Z, Peng F and Zhang P 2019 Recent advances in metal sulfides: from controlled fabrication to electrocatalytic, photocatalytic and photoelectrochemical water splitting and beyond *Chem. Soc. Rev.* **48** 4178–280
[53] Ganguly P, Harb M, Cao Z, Cavallo L, Breen A, Dervin S, Dionysiou D D and Pillai S C 2019 2D nanomaterials for photocatalytic hydrogen production *ACS Energy Lett.* **4** 1687–709
[54] Gao E, Lin S-Z, Qin Z, Buehler M J, Feng X-Q and Xu Z 2018 Mechanical exfoliation of two-dimensional materials *J. Mech. Phys. Solids* **115** 248–62
[55] Novoselov K S, Geim A K, Morozov S V, Jiang D, Zhang Y, Dubonos S V, Grigorieva I V and Firsov A A 2004 Electric field effect in atomically thin carbon films *Science* **306** 666–9
[56] Li H, Lu G, Wang Y, Yin Z, Cong C, He Q, Wang L, Ding F, Yu T and Zhang H 2013 Mechanical exfoliation and characterization of single- and few-layer nanosheets of WSe2, TaS2, and TaSe2 *Small* **9** 1974–81
[57] Novoselov K S, Jiang D, Schedin F, Booth T J, Khotkevich V V, Morozov S V and Geim A K 2005 Two-dimensional atomic crystals *Proc. Natl Acad. Sci. USA* **102** 10451
[58] An S-J, Kim Y H, Lee C, Park D Y and Jeong M S 2018 Exfoliation of transition metal dichalcogenides by a high-power femtosecond laser *Sci. Rep.* **8** 12957
[59] Yu Y, Huang S-Y, Li Y, Steinmann S N, Yang W and Cao L 2014 Layer-dependent electrocatalysis of MoS2 for hydrogen evolution *Nano Lett.* **14** 553–8
[60] He H *et al* 2016 MoS2/TiO2 edge-on heterostructure for efficient photocatalytic hydrogen evolution *Adv. Energy Mater.* **6** 1600464
[61] Nicolosi V, Chhowalla M, Kanatzidis M G, Strano M S and Coleman J N 2013 Liquid exfoliation of layered materials *Science* **340** 1226419
[62] Coleman J N *et al* 2011 Two-dimensional nanosheets produced by liquid exfoliation of layered materials *Science* **331** 568–71
[63] Zhang Y, Yao Y, Sendeku M G, Yin L, Zhan X, Wang F, Wang Z and He J 2019 Recent progress in CVD growth of 2D transition metal dichalcogenides and related heterostructures *Adv. Mater.* **31** 1901694
[64] Li X L and Li Y D 2003 Formation of MoS2 inorganic fullerenes (IFs) by the reaction of MoO3 nanobelts and S *Chem. Eur. J.* **9** 2726–31
[65] Zhang Y *et al* 2014 Dendritic, transferable, strictly monolayer MoS2 flakes synthesized on SrTiO3 single crystals for efficient electrocatalytic applications *ACS Nano* **8** 8617–24
[66] Shi J *et al* 2017 Two-dimensional metallic tantalum disulfide as a hydrogen evolution catalyst *Nat. Commun.* **8** 958
[67] Zhang X, Ma G and Wang J 2019 Hydrothermal synthesis of two-dimensional MoS2 and its applications *Tungsten* **1** 59–79
[68] Chen X and Fan R 2001 Low-temperature hydrothermal synthesis of transition metal dichalcogenides *Chem. Mater.* **13** 802–5
[69] He H Y 2017 Efficient hydrogen evolution activity of 1T-MoS2/Si-doped TiO2 nanotube hybrids *Int. J. Hydrogen Energy* **42** 20739–48
[70] Xu X, Fan Z, Ding S, Yu D and Du Y 2014 Fabrication of MoS2 nanosheet@TiO2 nanotube hybrid nanostructures for lithium storage *Nanoscale* **6** 5245–50
[71] Zhang X *et al* 2017 MoS2/carbon nanotube core–shell nanocomposites for enhanced nonlinear optical performance *Chem. Eur. J.* **23** 3321–7
[72] Li Y, Wang H, Xie L, Liang Y, Hong G and Dai H 2011 MoS2 nanoparticles grown on graphene: an advanced catalyst for the hydrogen evolution reaction *J. Am. Chem. Soc.* **133** 7296–9
[73] Wang H, Kong D, Johanes P, Cha J J, Zheng G, Yan K, Liu N and Cui Y 2013 MoSe2 and WSe2 nanofilms with vertically aligned molecular layers on curved and rough surfaces *Nano Lett.* **13** 3426–33
[74] Hu J, Huang B, Zhang C, Wang Z, An Y, Zhou D, Lin H, Leung M K H and Yang S 2017 Engineering stepped edge surface structures of MoS2 sheet stacks to accelerate the hydrogen evolution reaction *Energy Environ. Sci.* **10** 593–603
[75] Wang A, Zhang M, Li H, Wu F, Yan K and Xiao J 2019 Combination of theory and experiment achieving a rational design of electrocatalysts for hydrogen evolution on the hierarchically mesoporous CoS2 microsphere *J. Phys. Chem.* C **123** 13428–33
[76] Voiry D, Salehi M, Silva R, Fujita T, Chen M, Asefa T, Shenoy V B, Eda G and Chhowalla M 2013 Conducting MoS2 nanosheets as catalysts for hydrogen evolution reaction *Nano Lett.* **13** 6222–7
[77] Lukowski M A, Daniel A S, Meng F, Forticaux A, Li L and Jin S 2013 Enhanced hydrogen evolution catalysis from chemically exfoliated metallic MoS2 nanosheets *J. Am. Chem. Soc.* **135** 10274–7

[78] Liu B, Zhao Y-F, Peng H-Q, Zhang Z-Y, Sit C-K, Yuen M-F, Zhang T-R, Lee C-S and Zhang W-J 2017 Nickel–cobalt diselenide 3D mesoporous nanosheet networks supported on Ni foam: an all-pH highly efficient integrated electrocatalyst for hydrogen evolution *Adv. Mater.* **29** 1606521
[79] Voiry D *et al* 2013 Enhanced catalytic activity in strained chemically exfoliated WS2 nanosheets for hydrogen evolution *Nat. Mater.* **12** 850–5
[80] Yin Y *et al* 2017 Disorder engineering in 1T-MoSe2 nanosheets for enhanced hydrogen-evolution reaction *Adv. Mater.* **29** 1700311
[81] Kong D, Wang H, Lu Z and Cui Y 2014 CoSe2 nanoparticles grown on carbon fiber paper: an efficient and stable electrocatalyst for hydrogen evolution reaction *J. Am. Chem. Soc.* **136** 4897–900
[82] Li H *et al* 2016 Activating and optimizing MoS2 basal planes for hydrogen evolution through the formation of strained sulphur vacancies *Nat. Mater.* **15** 48–53
[83] Li J, Kang J, Cai Q, Hong W, Jian C, Liu W and Banerjee K 2017 Boosting hydrogen evolution performance of MoS2 by band structure engineering *Adv. Mater. Interfaces* **4** 1700303
[84] Li G *et al* 2016 All the catalytic active sites of MoS2 for hydrogen evolution *J. Am. Chem. Soc.* **138** 16632–8
[85] Dong L, Guo S, Wang Y, Zhang Q, Gu L, Pan C and Zhang J 2019 Activating MoS2 basal planes for hydrogen evolution through direct CVD morphology control *J. Mater. Chem.* A **7** 27603–11
[86] Tsai C, Li H, Park S, Park J, Han H S, Nørskov J K, Zheng X and Abild-Pedersen F 2017 Electrochemical generation of sulfur vacancies in the basal plane of MoS2 for hydrogen evolution *Nat. Commun.* **8** 15113
[87] Gao G, Xie X, Kang S, Lei Y, Trampert A and Cai L 2019 Toward heterostructured transition metal hybrids with highly promoted electrochemical hydrogen evolution *RSC Adv.* **9** 19924–9
[88] Geng S, Liu H, Yang W and Yu Y S 2018 Activating the MoS2 basal plane by controllable fabrication of pores for an enhanced hydrogen evolution reaction *Chem. Eur. J.* **24** 19075–80
[89] Yin Y *et al* 2016 Contributions of phase, sulfur vacancies, and edges to the hydrogen evolution reaction catalytic activity of porous molybdenum disulfide nanosheets *J. Am. Chem. Soc.* **138** 7965–72
[90] Merki D, Fierro S, Vrubel H and Hu X 2011 Amorphous molybdenum sulfide films as catalysts for electrochemical hydrogen production in water *Chem. Sci.* **2** 1262–7
[91] Wu L, Longo A, Dzade N Y, Sharma A, Hendrix M M R M, Bol A A, de Leeuw N H, Hensen E J M and Hofmann J P 2019 The origin of high activity of amorphous MoS2 in the hydrogen evolution reaction *ChemSusChem* **12** 4383–9
[92] Morales-Guio C G and Hu X 2014 Amorphous molybdenum sulfides as hydrogen evolution catalysts *Acc. Chem. Res.* **47** 2671–81
[93] Benck J D, Chen Z, Kuritzky L Y, Forman A J and Jaramillo T F 2012 Amorphous molybdenum sulfide catalysts for electrochemical hydrogen production: insights into the origin of their catalytic activity *ACS Catal.* **2** 1916–23
[94] Wang T, Zhuo J, Du K, Chen B, Zhu Z, Shao Y and Li M 2014 Electrochemically fabricated polypyrrole and MoSx copolymer films as a highly active hydrogen evolution electrocatalyst *Adv. Mater.* **26** 3761–6
[95] Merki D, Vrubel H, Rovelli L, Fierro S, Hu X and Fe C 2012 Ni ions promote the catalytic activity of amorphous molybdenum sulfide films for hydrogen evolution *Chem. Sci.* **3** 2515–25
[96] Kokko M, Bayerköhler F, Erben J, Zengerle R, Kurz P and Kerzenmacher S 2017 Molybdenum sulphides on carbon supports as electrocatalysts for hydrogen evolution in acidic industrial wastewater *Appl. Energy* **190** 1221–33
[97] Nguyen Q T, Nguyen P D, Nguyen D N, Truong Q D, Kim Chi T T, Ung T T D, Honma I, Liem N Q and Tran P D 2018 Novel amorphous molybdenum selenide as an efficient catalyst for hydrogen evolution reaction *ACS Appl. Mater. Interfaces* **10** 8659–65
[98] Carim A I, Saadi F H, Soriaga M P and Lewis N S 2014 Electrocatalysis of the hydrogen-evolution reaction by electrodeposited amorphous cobalt selenide films *J. Mater. Chem.* A **2** 13835–9
[99] Wang P, Wan L, Lin Y and Wang B 2019 MoS2 supported CoS2 on carbon cloth as a high-performance electrode for hydrogen evolution reaction *Int. J. Hydrogen Energy* **44** 16566–74
[100] Staszak-Jirkovský J *et al* 2016 Design of active and stable Co–Mo–Sx chalcogels as pH-universal catalysts for the hydrogen evolution reaction *Nat. Mater.* **15** 197–203
[101] Zhang H, Yang B, Wu X, Li Z, Lei L and Zhang X 2015 Polymorphic CoSe2 with mixed orthorhombic and cubic phases for highly efficient hydrogen evolution reaction *ACS Appl. Mater. Interfaces* **7** 1772–9
[102] Wang L, Hu P, Long Y, Liu Z and He X 2017 Recent advances in ternary two-dimensional materials: synthesis, properties and applications *J. Mater. Chem.* A **5** 22855–76
[103] Kiran V, Mukherjee D, Jenjeti R N and Sampath S 2014 Active guests in the MoS2/MoSe2 host lattice: efficient hydrogen evolution using few-layer alloys of MoS2(1−x)Se2x *Nanoscale* **6** 12856–63
[104] Konkena B, Masa J, Xia W, Muhler M and Schuhmann W 2016 MoSSe@reduced graphene oxide nanocomposite heterostructures as efficient and stable electrocatalysts for the hydrogen evolution reaction *Nano Energy* **29** 46–53
[105] Liu K, Wang F, Xu K, Shifa T A, Cheng Z, Zhan X and He J 2016 CoS2xSe2(1−x) nanowire array: an efficient ternary electrocatalyst for the hydrogen evolution reaction *Nanoscale* **8** 4699–704
[106] Xu K, Wang F, Wang Z, Zhan X, Wang Q, Cheng Z, Safdar M and He J 2014 Component-Controllable WS2(1–x)Se2x Nanotubes for efficient hydrogen evolution reaction *ACS Nano* **8** 8468–76
[107] Zhang Y, Liu K, Wang F, Shifa T A, Wen Y, Wang F, Xu K, Wang Z, Jiang C and He J 2017 Dendritic growth of monolayer ternary WS2(1−x)Se2x flakes for enhanced hydrogen evolution reaction *Nanoscale* **9** 5641–7
[108] Fu Q, Yang L, Wang W, Han A, Huang J, Du P, Fan Z, Zhang J and Xiang B 2015 Synthesis and enhanced electrochemical catalytic performance of monolayer WS2(1–x) se2x with a tunable band gap *Adv. Mater.* **27** 4732–8
[109] Wang F *et al* 2015 Enhanced electrochemical H2 evolution by few-layered metallic WS2(1−x)Se2x nanoribbons *Adv. Funct. Mater.* **25** 6077–83
[110] Xia C, Liang H, Zhu J, Schwingenschlögl U and Alshareef H N 2017 Active edge sites engineering in nickel cobalt selenide solid solutions for highly efficient hydrogen evolution *Adv. Energy Mater.* **7** 1602089
[111] Oyama S T, Wang X, Lee Y K and Chun W J 2004 Active phase of Ni2P/SiO2 in hydroprocessing reactions *J. Catal.* **221** 263–73
[112] Senevirathne K, Burns A W, Bussell M E and Brock S L 2007 Synthesis and characterization of discrete nickel phosphide nanoparticles: effect of surface ligation chemistry on catalytic hydrodesulfurization of thiophene *Adv. Funct. Mater.* **17** 3933–9
[113] Oyama S T 2003 Novel catalysts for advanced hydroprocessing: transition metal phosphides *J. Catal.* **216** 343–52
[114] Oyama S T, Gott T, Zhao H and Lee Y-K 2009 Transition metal phosphide hydroprocessing catalysts: A review *Catal. Today* **143** 94–107
[115] Liu P and Rodriguez J A 2005 Catalysts for hydrogen evolution from the [NiFe] hydrogenase to the Ni2P(001) surface: the importance of ensemble effect *J. Am. Chem. Soc.* **127** 14871–8

[116] Liang Z, Zhong X, Li T, Chen M and Feng G 2019 DFT study on the hydrogen evolution reaction for different facets of Co2P *ChemElectroChem* **6** 260–7
[117] Cabán-Acevedo M, Stone M L, Schmidt J R, Thomas J G, Ding Q, Chang H-C, Tsai M-L, He J-H and Jin S 2015 Efficient hydrogen evolution catalysis using ternary pyrite-type cobalt phosphosulphide *Nat. Mater.* **14** 1245–51
[118] Wu T, Stone M L, Shearer M J, Stolt M J, Guzei I A, Hamers R J, Lu R, Deng K, Jin S and Schmidt J R 2018 Crystallographic facet dependence of the hydrogen evolution reaction on CoPS: theory and experiments *ACS Catal.* **8** 1143–52
[119] Popczun E J, Read C G, Roske C W, Lewis N S and Schaak R E 2014 Highly active electrocatalysis of the hydrogen evolution reaction by cobalt phosphide nanoparticles *Angew. Chem. Int. Ed.* **53** 5427–30
[120] Saadi F H, Carim A I, Verlage E, Hemminger J C, Lewis N S and Soriaga M P 2014 CoP as an acid-stable active electrocatalyst for the hydrogen-evolution reaction: electrochemical synthesis, interfacial characterization and performance evaluation *J. Phys. Chem.* C **118** 29294–300
[121] Sumboja A, An T, Goh H Y, Lübke M, Howard D P, Xu Y, Handoko A D, Zong Y and Liu Z 2018 One-step facile synthesis of cobalt phosphides for hydrogen evolution reaction catalysts in acidic and alkaline medium *ACS Appl. Mater. Interfaces* **10** 15673–80
[122] Hu Z, Yuan L, Liu Z, Shen Z and Yu J C 2016 An elemental phosphorus photocatalyst with a record high hydrogen evolution efficiency *Angew. Chem. Int. Ed.* **55** 9580–5
[123] Zhu M, Kim S, Mao L, Fujitsuka M, Zhang J, Wang X and Majima T 2017 Metal-free photocatalyst for H2 evolution in visible to near-infrared region: black phosphorus/graphitic carbon nitride *J. Am. Chem. Soc.* **139** 13234–42
[124] Tian B, Tian B, Smith B, Scott M C, Hua R, Lei Q and Tian Y 2018 Supported black phosphorus nanosheets as hydrogen-evolving photocatalyst achieving 5.4% energy conversion efficiency at 353 K *Nat. Commun.* **9** 1397
[125] Popczun E J, McKone J R, Read C G, Biacchi A J, Wiltrout A M, Lewis N S and Schaak R E 2013 Nanostructured nickel phosphide as an electrocatalyst for the hydrogen evolution reaction *J. Am. Chem. Soc.* **135** 9267–70
[126] Kucernak A R J and Naranammalpuram Sundaram V N 2014 Nickel phosphide: the effect of phosphorus content on hydrogen evolution activity and corrosion resistance in acidic medium *J. Mater. Chem.* A **2** 17435–45
[127] Liu Q, Tian J, Cui W, Jiang P, Cheng N, Asiri A M and Sun X 2014 Carbon nanotubes decorated with CoP nanocrystals: a highly active non-noble-metal nanohybrid electrocatalyst for hydrogen evolution *Angew. Chem. Int. Ed.* **53** 6710–4
[128] Tian J, Liu Q, Asiri A M and Sun X 2014 Self-supported nanoporous cobalt phosphide nanowire arrays: an efficient 3D hydrogen-evolving cathode over the wide range of pH 0–14 *J. Am. Chem. Soc.* **136** 7587–90
[129] Pu Z, Liu Q, Jiang P, Asiri A M, Obaid A Y and Sun X 2014 CoP nanosheet arrays supported on a Ti plate: an efficient cathode for electrochemical hydrogen evolution *Chem. Mater.* **26** 4326–9
[130] Gu S, Du H, Asiri A M, Sun X and Li C M 2014 Three-dimensional interconnected network of nanoporous CoP nanowires as an efficient hydrogen evolution cathode *Phys. Chem. Chem. Phys.* **16** 16909–13
[131] Huang Z, Chen Z, Chen Z, Lv C, Humphrey M G and Zhang C 2014 Cobalt phosphide nanorods as an efficient electrocatalyst for the hydrogen evolution reaction *Nano Energy* **9** 373–82
[132] Pan Y, Lin Y, Chen Y, Liu Y and Liu C 2016 Cobalt phosphide-based electrocatalysts: synthesis and phase catalytic activity comparison for hydrogen evolution *J. Mater. Chem.* A **4** 4745–54
[133] Yang H, Zhang Y, Hu F and Wang Q 2015 Urchin-like CoP nanocrystals as hydrogen evolution reaction and oxygen reduction reaction dual-electrocatalyst with superior stability *Nano Lett.* **15** 7616–20
[134] Jiang P, Liu Q, Ge C, Cui W, Pu Z, Asiri A M and Sun X 2014 CoP nanostructures with different morphologies: synthesis, characterization and a study of their electrocatalytic performance toward the hydrogen evolution reaction *J. Mater. Chem.* A **2** 14634–40
[135] Zhang X, Han Y, Huang L and Dong S 2016 3D graphene aerogels decorated with cobalt phosphide nanoparticles as electrocatalysts for the hydrogen evolution reaction *ChemSusChem* **9** 3049–53
[136] Son C Y, Kwak I H, Lim Y R and Park J 2016 FeP and FeP2 nanowires for efficient electrocatalytic hydrogen evolution reaction *Chem. Commun.* **52** 2819–22
[137] Yan H, Jiao Y, Wu A, Tian C, Zhang X, Wang L, Ren Z and Fu H 2016 Cluster-like molybdenum phosphide anchored on reduced graphene oxide for efficient hydrogen evolution over a broad pH range *Chem. Commun.* **52** 9530–3
[138] Morales-Guio C G, Stern L-A and Hu X 2014 Nanostructured hydrotreating catalysts for electrochemical hydrogen evolution *Chem. Soc. Rev.* **43** 6555–69
[139] Xiao P, Sk M A, Thia L, Ge X, Lim R J, Wang J-Y, Lim K H and Wang X 2014 Molybdenum phosphide as an efficient electrocatalyst for the hydrogen evolution reaction *Energy Environ. Sci.* **7** 2624–9
[140] Kibsgaard J and Jaramillo T F 2014 Molybdenum phosphosulfide: an active, acid-stable, earth-abundant catalyst for the hydrogen evolution reaction *Angew. Chem. Int. Ed.* **53** 14433–7
[141] Sultana U K and O'Mullane A P 2018 Electrochemical formation of amorphous molybdenum phosphosulfide for enabling the hydrogen evolution reaction in alkaline and acidic media *ACS Appl. Energy Mater.* **1** 2849–58
[142] Huang Y, Song X, Deng J, Zha C, Huang W, Wu Y and Li Y 2019 Ultra-dispersed molybdenum phosphide and phosphosulfide nanoparticles on hierarchical carbonaceous scaffolds for hydrogen evolution electrocatalysis *Appl. Catal.* B **245** 656–61
[143] Shi Z *et al* 2017 Phosphorus-Mo2C@carbon nanowires toward efficient electrochemical hydrogen evolution: composition, structural and electronic regulation *Energy Environ. Sci.* **10** 1262–71
[144] Fang S-L, Chou T-C, Samireddi S, Chen K-H, Chen L-C and Chen W-F 2017 Enhanced hydrogen evolution reaction on hybrids of cobalt phosphide and molybdenum phosphide *Royal Soc. Open Sci.* **4** 161016
[145] Guan C, Xiao W, Wu H, Liu X, Zang W, Zhang H, Ding J, Feng Y P, Pennycook S J and Wang J 2018 Hollow Mo-doped CoP nanoarrays for efficient overall water splitting *Nano Energy* **48** 73–80
[146] Jäger M O J, Morooka E V, Federici Canova F, Himanen L and Foster A S 2018 Machine learning hydrogen adsorption on nanoclusters through structural descriptors *Npj Comput. Mater.* **4** 37
[147] Quesne M G, Silveri F, de Leeuw N H and Catlow C R A 2019 Advances in sustainable catalysis: A computational perspective *Front. Chem.* **7** 182–182
[148] Pérez A E and Ribadeneira R 2018 Chapter 2: Modeling with DFT and chemical descriptors approach for the development of catalytic alloys for PEMFCs *Density Functional Theory*, ed D Glossman-Mitnik (Rijeka: IntechOpen) pp 33–54
[149] Saleheen M and Heyden A 2018 Liquid-phase modeling in heterogeneous catalysis *ACS Catal.* **8** 2188–94
[150] Ping Y, Sundararaman R and Goddard Iii W A 2015 Solvation effects on the band edge positions of photocatalysts from first principles *Phys. Chem. Chem. Phys.* **17** 30499–509

[151] Skúlason E, Karlberg G S, Rossmeisl J, Bligaard T, Greeley J, Jónsson H and Nørskov J K 2007 Density functional theory calculations for the hydrogen evolution reaction in an electrochemical double layer on the Pt(111) electrode *Phys. Chem. Chem. Phys.* **9** 3241–50
[152] Gono P, Ambrosio F and Pasquarello A 2019 Effect of the solvent on the oxygen evolution reaction at the TiO2–water interface *J. Phys. Chem.* C **123** 18467–74
[153] Hawlitzky M, Horbach J, Ispas S, Krack M and Binder K 2008 Comparative classical and 'ab initio' molecular dynamics study of molten and glassy germanium dioxide *J. Phys.: Condens. Matter* **20** 285106
[154] Zhang J, Xu F, Hong Y, Xiong Q and Pan J 2015 A comprehensive review on the molecular dynamics simulation of the novel thermal properties of graphene *RSC Adv.* **5** 89415–26
[155] Paquet E and Viktor H L 2018 Computational methods for Ab initio molecular dynamics *Adv. Chem.* **2018** 9839641
[156] Kronberg R, Lappalainen H and Laasonen K 2020 Revisiting the Volmer–Heyrovský mechanism of hydrogen evolution on a nitrogen doped carbon nanotube: constrained molecular dynamics versus the nudged elastic band method *Phys. Chem. Chem. Phys.* **22** 10536–49
[157] Cheng J, VandeVondele J and Sprik M 2014 Identifying trapped electronic holes at the aqueous TiO2 interface *J. Phys. Chem.* C **118** 5437–44
[158] Van den Bossche M, Skúlason E, Rose-Petruck C and Jónsson H 2019 Assessment of constant-potential implicit solvation calculations of electrochemical energy barriers for H2 evolution on Pt *J. Phys. Chem.* C **123** 4116–24
[159] Rossmeisl J, Skúlason E, Björketun M E, Tripkovic V and Nørskov J K 2008 Modeling the electrified solid–liquid interface *Chem. Phys. Lett.* **466** 68–71
[160] Skúlason E, Tripkovic V, Björketun M E, Gudmundsdóttir S, Karlberg G, Rossmeisl J, Bligaard T, Jónsson H and Nørskov J K 2010 Modeling the electrochemical hydrogen oxidation and evolution reactions on the basis of density functional theory calculations *J. Phys. Chem.* C **114** 18182–97
[161] Chang L, Cheng D, Sementa L and Fortunelli A 2018 Hydrogen evolution reaction (HER) on Au@Ag ultrananoclusters as electro-catalysts *Nanoscale* **10** 17730–7
[162] Rupp M, Tkatchenko A, Müller K-R and von Lilienfeld O A 2012 Fast and accurate modeling of molecular atomization energies with machine learning *Phys. Rev. Lett.* **108** 058301
[163] Huo H A and Rupp M A 2017 Unified representation of molecules and crystals for machine learning (arXiv:1704.06439v3)
[164] De S, Bartók A P, Csányi G and Ceriotti M 2016 Comparing molecules and solids across structural and alchemical space *Phys. Chem. Chem. Phys.* **18** 13754–69
[165] Bartók A P, Kondor R and Csányi G 2013 On representing chemical environments *Phys. Rev.* B **87** 184115
[166] Huang B, Xiao L, Lu J and Zhuang L 2016 Spatially resolved quantification of the surface reactivity of solid catalysts *Angew. Chem. Int. Ed.* **55** 6239–43
[167] Fukui K 1982 Role of frontier orbitals in chemical reactions *Science* **218** 747–54
[168] Ran N, Qiu W, Song E, Wang Y, Zhao X, Liu Z and Liu J 2020 Bond electronegativity as hydrogen evolution reaction catalyst descriptor for transition metal (TM = Mo, W) dichalcogenides *Chem. Mater.* **32** 1224–34
[169] Hu G, Tang Q and Jiang D-E 2016 CoP for hydrogen evolution: implications from hydrogen adsorption *Phys. Chem. Chem. Phys.* **18** 23864–71
[170] Kyriakou G, Boucher M B, Jewell A D, Lewis E A, Lawton T J, Baber A E, Tierney H L, Flytzani-Stephanapoulos M and Sykes C H 2012 Isolated metal atom geometries as a strategy for selective heterogenous hydrogenations *Science* **335** 1209–12
[171] Liu X, Zhou W, Yang L, Li L, Zhang Z, Ke Y and Chen S 2015 Nitrogen and sulfur co-doped porous carbon derived from human hair as highly efficient metal-free electrocatalysts for hydrogen evolution reactions *J. Mater. Chem.* A **3** 8840–6
[172] Anjum M A R and Lee J S 2017 Sulfur and nitrogen dual-doped molybdenum phosphide nanocrystallites as an active and stable hydrogen evolution reaction electrocatalyst in acidic and alkaline media *ACS Catal.* **7** 3030–8
[173] Ge L, Han C, Xiao X, Guo L and Li Y 2013 Enhanced visible light photocatalytic hydrogen evolution of sulfur-doped polymeric g-C3N4 photocatalysts *Mater. Res. Bull.* **48** 3919–25
[174] Hao X, Zhou J, Cui Z, Wang Y, Wang Y and Zou Z 2018 Zn-vacancy mediated electron-hole separation in ZnS/g-C3N4 heterojunction for efficient visible-light photocatalytic hydrogen production *Appl. Catal.* B **229** 41–51
[175] Gholamvand Z *et al* 2016 Comparison of liquid exfoliated transition metal dichalcogenides reveals MoSe2 to be the most effective hydrogen evolution catalyst *Nanoscale* **8** 5737–49
[176] Wang F, Li Y, Shifa T A, Liu K, Wang F, Wang Z, Xu P, Wang Q and He J 2016 Selenium-enriched nickel selenide nanosheets as a robust electrocatalyst for hydrogen generation *Angew. Chem. Int. Ed.* **55** 6919–24
[177] Tang H, Dou K, Kaun -C-C, Kuang Q and Yang S 2014 MoSe2 nanosheets and their graphene hybrids: synthesis, characterization and hydrogen evolution reaction studies *J. Mater. Chem.* A **2** 360–4
[178] Bhat K S and Nagaraja H S 2018 Nickel selenide nanostructures as an electrocatalyst for hydrogen evolution reaction *Int. J. Hydrogen Energy* **43** 19851–63
[179] Hou Y, Lohe M R, Zhang J, Liu S, Zhuang X and Feng X 2016 Vertically oriented cobalt selenide/NiFe layered-double-hydroxide nanosheets supported on exfoliated graphene foil: an efficient 3D electrode for overall water splitting *Energy Environ. Sci.* **9** 478–83
[180] Jiang K, Liu B, Luo M, Ning S, Peng M, Zhao Y, Lu Y-R, Chan T-S, de Groot F M F and Tan Y 2019 Single platinum atoms embedded in nanoporous cobalt selenide as electrocatalyst for accelerating hydrogen evolution reaction *Nat. Commun.* **10** 1743
[181] Guo S, Deng Z, Li M, Jiang B, Tian C, Pan Q and Fu H 2016 Phosphorus-doped carbon nitride tubes with a layered micro-nanostructure for enhanced visible-light photocatalytic hydrogen evolution *Angew. Chem. Int. Ed.* **55** 1830–4